Research Paper

Quantitative analysis and phase assemblage of basic oxygen furnace slag hydration

W. Franco Santos [a,*], K. Schollbach [a], S. Melzer [b], S.R. van der Laan [a,b], H.J.H. Brouwers [a]

[a] Department of the Built Environment, Eindhoven University of Technology, P.O. Box 513, 5600 MB Eindhoven, the Netherlands
[b] Tata Steel, R&D, Microstructure & Surface Characterization (MSC), P.O. Box 10.000, 1970 CA IJmuiden, the Netherlands

HIGHLIGHTS

- The hydration product of the same material with different sizes varies in amount and composition.
- It is calculated how much each of the original slag phases contributes to the formation of the hydration product.
- Divalent Mg, Mn, and Fe from wüstite are controlling the hydrotalcite formation.
- The oxidation of Fe^{2+} from wüstite, in a reaction consuming portlandite, contributes to hydrogarnet formation.
- The new hydrations products hydrogarnets and C-S-H gel could immobilize the heavy metals V and Cr.

GRAPHICAL ABSTRACT
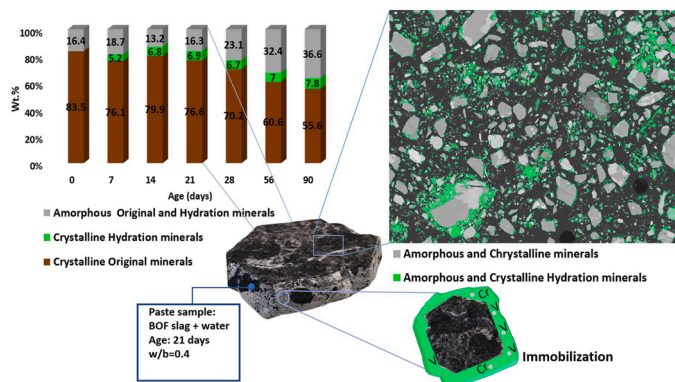
ARTICLE INFO

Editor: Feng Xiao

ABSTRACT

Basic oxygen furnace (BOF) slag from steelmaking could be applied as a binder in building materials, reducing the CO_2 footprint and solid waste, which is relevant for industrial waste management and circular economy. However, its use is mostly restricted because its hydraulic activity is poorly understood. The BOF slag was hydrated in this study, and its reaction products were systematically characterized using XRD, QXRD, and SEM/EDX-based phase mapping. Internal consistency checks of the data were performed between the analytical techniques. The results revealed that the composition of the amorphous hydration products could be identified and quantified, and the main hydration products were hydrogarnets and C-S-H gel. An extended milling process significantly improved the reactivity, and all the major slag phases, including wüstite, participated in the reaction. Brownmillerite formed hydrogarnets during the first 7 days of hydration. The new hydration products contributed to the immobilization of vanadium and chromium. Particle size played an important role in the amount of C_2S reacting, the composition of the hydrogarnets and C-S-H gel, their proportions, and the immobilization capacity. Based on the findings, an overall hydration reaction was developed.

---

* Corresponding author.
  E-mail address: w.franco.santos@tue.nl (W.F. Santos).

1. Introduction

Basic oxygen furnace (BOF) slag, also referred to as converter steel slag [1,2], is the main solid waste by-product of the steelmaking industry. It is generated during the refinement of pig iron to raw steel [3–5]. The worldwide crude steel production was around 1864 million tons in 2020 [6]. For each ton of crude steel produced, approximately 100–150 kg of BOF slag is generated [7]. In Europe, 72.4% of BOF slag is recovered and used for low-end applications such as aggregates in concrete and backfill materials [8–11]. However, in other parts of the world, most BOF slag piles up in landfills [12], resulting in serious land occupation problems, pollution, and resource waste.

The continued demand for cement-based materials by the construction industry leads to the intense exploitation of natural resources and to high CO_2 emissions [13]. As a strategy to mitigate this problem, BOF slag has been researched as an alternative material [4,14–17]. Using this by-product of the steel industry as an efficient alternative to ordinary Portland cement (OPC) would be a significant contribution to the circular economy, thereby increasing the rational utilization rate of resources. While the concrete sector may provide a promising application for BOF slag, it has been reported that BOF slag has low reactivity and can cause environmental problems as a consequence of the potential leaching of chromium (Cr) [19–21] and vanadium (V). In particular, V leaching can lead to concentrations up to and exceeding twice the limit value specified in the European environmental legislation [20], which restricts the use of BOF slag in sustainable developments.

The main phases of BOF slag are brownmillerite (Ca_2 $(Fe,Al)_2O_5$), wüstite $(Fe,Mg)O$, and the α'- and β- polymorphs of dicalcium silicate Ca_2SiO_4 (also known as C_2S) [24,25]. Of the constituent, the C_2S typically account for approximately 50% of the composition. These phases should be considered to participate in the reaction of BOF slag with water. Furthermore, it is known that C_2S phases incorporate V, which may be immobilized in the C-S-H gel after hydration [26]. Literature also shows that heavy metals can be immobilized in hydrogarnets [22]. Therefore, V and Cr can potentially be immobilized if BOF slag can form a sufficient amount of C-S-H gel and hydrogarnets during hydration. Therefore, good knowledge of the hydration mechanisms of BOF slag is necessary for the effective future use of this by-product [23].

The unravelling of hydration systems places great demands on material characterization. Researchers have combined quantitative microscopy and XRD to determine the reactions of cementitious binder components [27,28]. However, complementary methods are also needed for an in-depth study into the compositions of the hydration products of BOF slag. Few studies have focused on a quantitative assessment of the hydration reactions in a simple BOF slag system. To date, knowledge of the reactive phases and their contribution to the formation of new phases in the BOF slag hydration system is lacking.

Researchers have extensively reviewed the potential applications of BOF slags [16,18,29,30]. Kriskova et al. [31] indicated that structural changes could occur during the milling of steel slag, such as crystalline phases becoming amorphous [32], although a detailed quantification of the observed effects was not provided. The studies of Wang et al. and Zhu et al. found new reaction products, C-S-H gel and $Ca(OH)_2$, while improving the hydration of steel slag by increasing the temperature and adding NaOH [8] as well as grinding aids [33]. Hou and Liu [34] later improved the hydration by autoclaving and found the same hydration products. However, in these investigations, the hydration products, the overall reactivity, and the hydration reactions were not quantified. Nevertheless, understanding the hydration of the BOF slag system is fundamental.

Developing a new binder based on BOF slag places great demands on the characterization of the material and its hydration products. Therefore, there is a need for an in-depth investigation combining complementary methods to understand the actual composition of the hydration products of BOF slag. The first stage of explaining the mechanisms of hydration will contribute to optimizing the design of materials using BOF slag as a sustainable binder.

Following the above reasoning, in this study, we focused on a systematic investigation of the hydration of BOF slag. The hydration product composition and its phase proportions were assessed for two BOF slag particle sizes. In-depth physical and chemical characterization of the hydration products was conducted using thermogravimetric analysis (TGA), quantitative X-ray diffraction (QXRD), and SEM/EDX-based phase mapping using PARC software to obtain chemical and mineral compositions [35,36]. In parallel, an extensive comparison of PARC with XRF and QXRD was performed, quantifying deviations using the least squares (LSQ) method to verify internal data consistency. The investigation consisted of a time series of hydration progress, providing both the reaction kinetics and the evolution of the crystalline and amorphous phases. The links between the mineralogy of BOF slag, particle size, and hydration progress enable findings that are fundamental to understanding the BOF slag hydration system on its own before adding chemicals or admixtures in order to open new possibilities for the valorization of BOF slag.

2. Materials and methods

2.1. Materials

The BOF slag used in this study was provided by Tata Steel (IJmuiden, The Netherlands). The BOF slag is produced in heats of approximately 30 tons, with the refinement of 300 tons of hot metal and scrap to produce steel. After the refinement process, the BOF slag is poured into open pits, followed by secondary water cooling. Five heats of slag are cooled together in one pit for around 24 h and subsequently excavated and gathered in intermediate storage until metal recovery processing. During metal recovery on a batch of ~200 BOF slag heats, a representative sampling of 200 kg was performed on the processing stream of the 0–25 mm size fraction. Subsequently, the material was dried, sieved, and crushed to obtain 100 kg of 2–3 mm representative average production slag. The slag was stored in air-tight plastic drums to prevent carbonation. The material below 2 mm was not used in this research to avoid the influence of smaller, often carbonated particles in previous results. This information was provided by Tata Steel.

The grinding procedure was performed in the university laboratory using a Retsch RS 300 XL disc mill at a constant speed of 912 min^{-1} and a grinding jar volume of 2 l. To determine the effect of particle size on hydration kinetics, two particle sizes were chosen; the larger (D(50) = 58 μm) was designated as S-58 with a milling time duration of 5 min for an input of 1.5 kg and the smaller (D (50) = 16 μm) S-16, with a milling time duration of 15 min for an input of 1 kg.

The particle size distribution (PSD) was obtained by laser light scattering (LLS) technique using a Malvern Mastersizer 2000® PSD analyzer (Fig. 1). The specific surface area (SSA) of the BOF slag was measured by nitrogen adsorption (Tristar II 3020 V1.03 Series micrometre and Brunauer-Emmett-Teller -BET) methods, applying nitrogen at 77 K [37]. The SSA of the milled material increases significantly after longer milling, from a value of 0.5 m^2/g to 1.5 m^2/g.

The elemental composition of the BOF slag was determined by X-ray fluorescence (XRF) and was reported as oxide percentages. The analysis was performed on a fused bead with an XRF spectrometer from PANalytical (Epsilon 3 range, standardless OMNIAN method). The loss of ignition was evaluated beforehand by heating the sample to 1000 ℃ for 1 h. The chemical composition of the BOF slag is listed in Table 1. As expected, it is mainly composed of CaO, Fe_2O_3, SiO_2, and MgO, while Al_2O_3, TiO_2, V_2O_5, and Cr_2O are present as minor constituents. The contents of Fe_2O_3 and MgO are significantly higher than those in Portland cement, whereas the CaO content is lower. When BOF slag was heated in air to 1000 ℃ for loss of ignition, a mass gain of 1.7 wt% was induced as a consequence of the oxidation of metallic or divalent iron and manganese. When the non-hydrated sample was tested for TGA in a continuous N_2 flow environment, the total weight loss of 0.92 wt% was
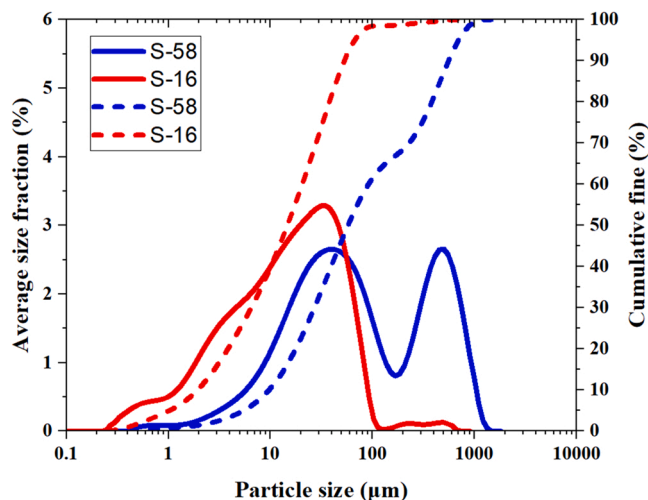
Fig. 1. Cumulative finer distributions and particle size distributions of S-16 and S-58. Color should be used in print.

recorded instead. The specific density measured by the Helium pycnometer (AccuPyc II 1340) for the BOF slag was 4.0 g/cm^3.

2.2. Methods

All hydrated BOF slag samples of S-16 and S-58 were prepared by mixing with water (w/s = 0.4) and sealed in plastic cups for 7–14–21–28–56 and 90 days of curing. After curing, the samples were crushed to powder, and hydration was stopped. Next, the samples were placed in alcohol (isopropanol) for 24 h to stop hydration and dried in an oven at 60 °C for 24 h [38].

For Quantitative X-ray diffractograms (QXRD), 10 wt% of crystalline Si was added to the pre-milled samples as an internal standard, 7 ml cyclohexane was added as a grinding aid in a McCrone micronizer, milling for 20 min down to a grain size of < 10 μm. Subsequently, cyclohexane evaporated in a drying oven for 5 min at 70 °C, and the powder was back-loaded onto a metal sample holder. A Bruker D8 Endeavor X-ray diffractometer was used, with Cu radiation, a step size of 0.02, a LynxeyeXE-T detector, and fixed divergence slits of 0.5°. The phases were identified with the Bruker software DIFFRAC. EVA 4.3 using the ICDD PDF-2 database (Appendix C-Table C1) and quantified with the Bruker software Topas 5.0 [39] using the Rietveld method [40]. The crystal structures for the quantification were obtained from either the ICSD database (FIZ Karlsruhe) or the PDF-4 database.

The evolving heat of BOF slag hydration was investigated using a Tam Air isothermal calorimeter (TA Instruments) at 20 °C for 90 h. A water-to-slag ratio (w/b) of 0.4 was used for the milled material in the calorimeter tests, which was sufficient to cover the BOF slag fully.

For thermogravimetric analysis (TGA/DTG), a Jupiter STA 449 F1 from Netzsch, was used with a heating rate of 10 °C/min under a continuous N$_2$ flow up to 1000 °C. A stepwise method was used for phase quantification.

The mineralogy of the non-hydrated BOF slag samples and those hydrated after 21d was also analyzed using the PARC Software (Phase recognition and characterization) [24,41]. The samples were prepared by mounting them in epoxy (Struers EpoFix) and polishing them to a flat surface without the use of water. It was then coated with approximately 10 nm of carbon. The analysis is based on Scanning Electron Microscopy

(SEM) combined with EDX Spectral imaging (SI) using a JEOL JSM-7001 F SEM, equipped with two 30 mm^2 SDD detectors (Thermo Fisher Scientific) and NORAN–System7 hardware with NSS.3.3 software. The SEM accelerating voltage was 15 kV, and the beam current was 6.2 nA. The step size used for Spectral Imaging was 1 μm per pixel. Each field contained 512 × 382 data points. PARC enables the grouping of EDX spectra obtained from all measured pixels according to their elemental peaks above a predefined threshold and returns the amount of each phase (number of phase pixels) in area% and the average chemical composition of each phase. For the non-hydrated samples, 9 SI fields were stitched together (1.8 mm^2), and for the hydrated samples, 49 fields (9.6 mm^2) were used to obtain the lowest reasonable standard error. The degree of hydration (DOH) was calculated for the samples after 21d using EDX mappings from SEM, according to Kocaba et al. [42].

The LSQ method used as an internal consistency verification to compare PARC with XRF and QXRD is described in Appendix A.

Leaching tests of unreacted BOF slag, and S-58 and S-16 hydrated for 21 days, were conducted following EN 12457–2 (one-stage batch leaching test) [43]. The samples were crushed and sieved below 4 mm. This material was mixed with deionized water (0.055 Us/cm) using a liquid-to-solid ratio of 10 l/kg, and this mixture was placed in a dynamic shaker (ES-SM-30 by Edmund Buhler GmbH) for 24 h and vibrated at 250 rpm. After 24 h, the leachate was filtered using a filter paper with a pore diameter of 5 μm. The pH of the filtered leachate was measured with a Voltkraft PH-100ATC pH electrode. A small quantity of the leachate is then taken and filtered by use of a syringe filter with a pore diameter of 0.22 μm (Whatman) and acidified with ultra-pure Nitric acid (HNO$_3$). It was then analyzed by inductively coupled plasma optical emission spectrometry (ICP-OES; Spectroblue) according to NEN 6966 (NEN-EN 6966, 2005). The obtained element concentrations were compared with the legal limits specified in the Dutch Soil Quality Decree (DSQD) [44].

3. Results and discussion

3.1. Mineralogy of BOF slag

3.1.1. Quantitative X-ray diffraction (QXRD) analysis

The Rietveld quantification results of the powder X-ray diffraction (XRD) analyzes are presented in Table 2. The major crystalline phases of the starting slag (0d values) are brownmillerite (C$_4$AF), α'-C$_2$S, larnite (β-C$_2$S), wüstite and magnetite, with similar contents in S-16 as in S-58. Before hydration, both analyzes presented an amorphous phase, with 16.4 wt% in S-16 and 14.8 wt% in S-58. Because of the presence of wüstite with different Mg and Fe contents, two different wüstite compositions (Mg-rich and Fe-rich) were used for fitting. For brownmillerite, the crystal structure composed of Ca$_2$Fe$_{1.8}$Al$_{0.2}$O$_5$ was adopted for Rietveld refinement. Statistical criteria Rwp (R-weighted-profile) and GOF (goodness-of-fit) [45,46] of the measurements are listed in Table C2 (Appendix C). The amorphous content before hydration is unusual because BOF slag is known to be completely crystalline after solidification [47]. The appearance of amorphous content after milling suggests that the crystalline mineral phases partially become X-ray amorphous from grinding [48], an observation supported by the higher amorphous content in S-16 than in S-58. Additionally, the quantification could also be influenced by micro absorption effects caused by the existence of multiple phases of varying absorption contrast [49], affecting the accuracy of the determination of both the crystalline and amorphous components.

Table 1
Chemical composition of BOF slag measured by X-ray Fluorescence.

Oxide	MgO	Al$_2$O$_3$	SiO$_2$	P$_2$O$_5$	CaO	TiO$_2$	V$_2$O$_5$	Cr$_2$O$_3$	MnO	Fe$_2$O$_3$	GOI
Wt%	8.0	2.3	13.4	1.6	38.0	1.4	1.0	0.3	4.2	28.0	1.7

Table 2

Phase amounts for the BOF slag starting material non-hydrated and S-58 and S-16 in wt% and after hydration of 7,14,21,28,56, and 90 days determined by XRD. Corresponding 1σ error values on the pattern fit are given in Table C3(Appendix C).

Mineral	Composition	S-58							S-16							Crystal density g/cm³
		0d	7d	14d	21d	28d	56d	90d	0d	7d	14d	21d	28d	56d	90d	
Fe- Wüstite	Fe(Mg)O	6.6	7.3	6.8	7.3	6.0	4.5	4.3	8.2	6.3	6.3	6.9	6.1	4.4	4.2	5.9
Mg- Wüstite	Mg(Fe)O	11.9	12.5	11.4	11.7	10.9	8.8	8.4	12.1	10.8	11.3	9.5	9.0	8.2	7.6	4.7
Magnetite	Fe_3O_4	9.3	10.2	10.0	9.9	9.2	6.9	7.4	12.5	13.6	14.3	14.7	13.4	13.3	14.1	5.1
Brownmillerite	$Ca_2(Al, Fe)_2O_5$	16.3	15.0	14.5	14.3	13.5	12.1	11.4	17.2	13.3	13.5	14	12.4	11.9	11.1	4.0
β-C2S	Ca_2SiO_4	24.1	25.5	24.7	24.4	23.1	21.3	20.5	18.9	19.4	21.4	20.3	19.2	15.9	13.5	3.3
α'-C2S	Ca_2SiO_4	16.3	16.0	14.9	15.2	14.6	12.4	10.8	14.0	12.5	13.0	11.2	10.0	6.9	5.0	3.3
Lime	CaO	0.3	0.2	0.3	0.2	0.2	0.2	0.1	0.3	0.2	0.1	0.1	0.1	0.1	0.1	3.4
Portlandite	$Ca(OH)_2$	0.3	0.4	0.6	0.6	0.7	1.0	1.0	0.3	0.6	0.9	0.9	1.0	1.0	1.2	2.2
Calcite	$CaCO_3$	0.0	0.0	0.0	0.0	0.0	1.2	1.7	0.0	0.0	0.0	0.0	0.0	0.0	0.0	2.7
Fe-Katoite	$Ca_3(Al,Fe)_2(OH)_{12}$	0.0	1.9	2.0	2.4	2.2	2.8	2.8	0.0	4.4	5.5	5.4	5.3	5.9	6.5	2.6
Pyroaurite	$Mg_6Fe_2(CO_3)(OH)_{16} * 4(H_2O)$	0.0	1.2	1.2	1.0	1.0	0.7	0.4	0.0	0.2	0.4	0.6	0.4	0.1	0.1	2.1
Amorphous	Amorphous	14.8	9.8	13.6	13	18.7	28.1	31.0	16.4	18.9	13.2	16.3	23.2	32.4	36.7	-

3.1.2. Scanning electron microscopy (SEM) and PARC

Figs. 2a and b present the morphological features of S-58 and S-16 in an SEM back-scatter image of the embedded and polished particles. S-58 consists mostly of particles with sharp and irregular edges, whereas in S-16, particles appear more rounded, and agglomeration of fines [50] was observed. The PARC phase maps are shown in Fig. 2c for S-58 and Fig. 2d for S-16, with four different phases identified.

The results of the phase compositions (in wt% oxides) and amounts (in area%), as determined with PARC, based on the full spectral image of 9 SEM fields, are given in Table 3. The black (pixels) area referred to as 'embedding' is not included with the phase amounts. Different from XRD

analysis, the two C2S polymorphs α'-C2S and β-C2S can not be differentiated in PARC, as they have the same chemical composition. PARC analysis (Table 3) shows that the C2S phase contains minor amounts of Fe_2O_3, P_2O_5, V_2O_5, and TiO_2. This composition is different from the C2S present in cement clinker [51,52]. The second most common phase is $MgFeO_x$, followed by brownmillerite. $MgFeO_x$ refers to the phases formed by MgO and FeO, like wüstite and magnetite, which cannot be differentiated based on chemical composition. Brownmillerite is equivalent to the C4AF phase of the clinker. However, dominated by ferrite over alumina with Fe:Al = 2:1, containing substantial titania, minor silica and vanadate. The phase $CaO/CaCO_3/Ca(OH)_2$ is named this way
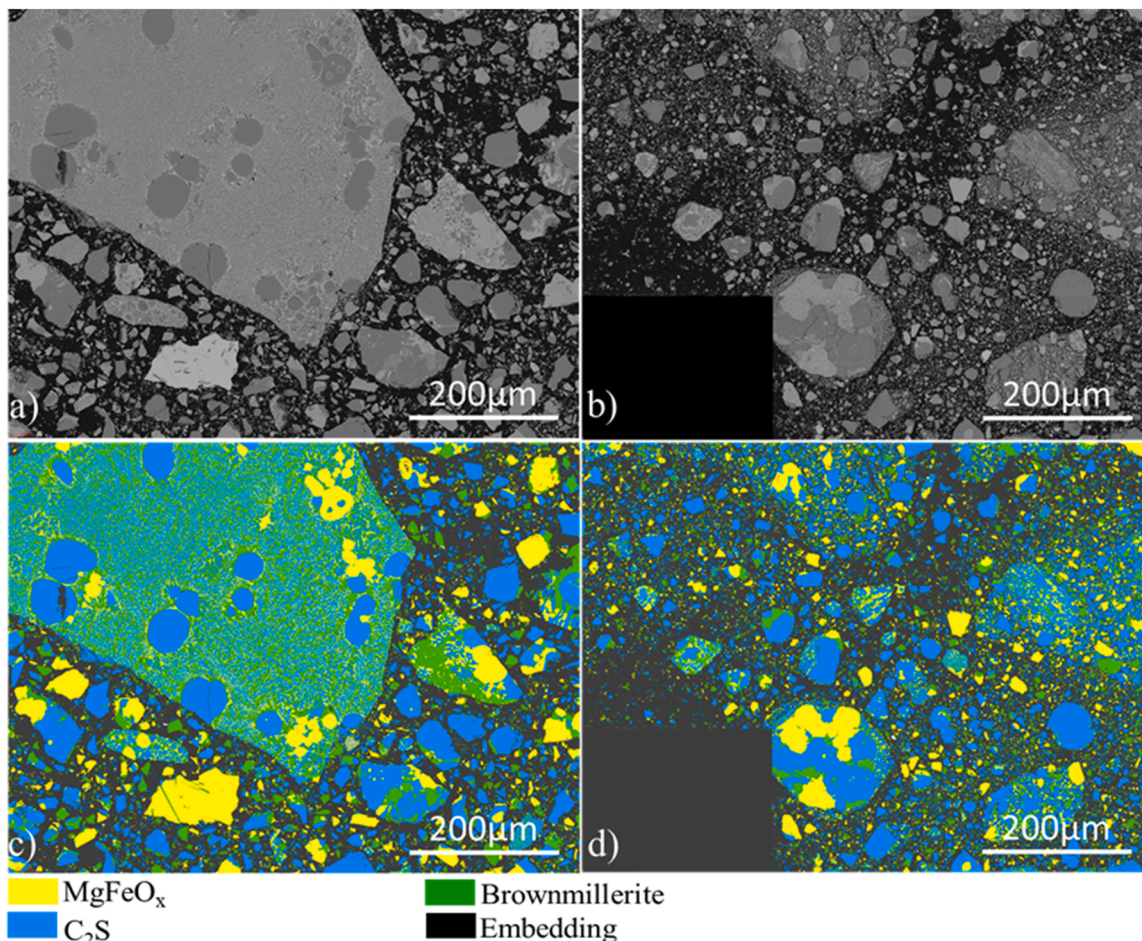

Fig. 2. SEM Back Scatter Electron (BSE) Image and PARC phase map of starting materials S-58(a and c) and S-16 (b and d). Color should be used in print.

Table 3

The average chemical composition and amount (area %) of phases identified in S-16 and S-58 with PARC.

Compound concentration %	MgFeOx		Brownmillerite		C2S		CaO /Ca (OH)$_2$/ CaCO$_3$	
	{Mg, Fe}		{Ca,Fe}		{Ca, Si}		{Ca}	
	Wüstite +Magnetite		Brownmillerite		β-C$_2$S + α'-C$_2$S		f-lime + Portlandite+Calcite	
	S-16	S-58	S-16	S-58	S-16	S-58	S-16	S-58
Na$_2$O	0.00	0.00	0	0	0.18	0.1	-	0
MgO	25.04	23.94	0.9	0.75	0.54	0.7	-	0.5
Al$_2$O$_3$	0.14	0.17	10.43	11.45	0.82	0.75	-	0
SiO$_2$	0.59	0.54	2.14	2.81	28.01	27.56	-	0.23
P$_2$O$_5$	0.02	0.02	0.15	0.23	3.27	3.38	-	0.17
SO$_3$	0.00	0.00	0	0.14	0.13	0.16	-	0.06
Cl	0.00	0.00	0.03	0.02	0.03	0.02	-	0.06
K$_2$O	0.00	0.00	0.05	0.04	0.04	0.04	-	0.17
CaO	2.22	2.02	42.32	42.78	60.61	59.29	-	85.78
TiO$_2$	0.04	0.04	5.58	4.68	1.1	0.95	-	0.25
V$_2$O$_5$	0.11	0.11	1.55	1.76	1.15	0.96	-	0.01
Cr$_2$O$_3^\dagger$	0.46	0.54	0.38	0.2	0.05	0.05	-	0
MnO	12.11	10.06	1.28	1.6	0.26	0.79	-	6.5
Fe$_2$O$_3$*	59.28	62.56	35.18	33.53	3.14	4.59	-	6.26
Amount Area%	22.6	22.5	19.51	26.09	57.93	51.37	0.0	0.05
σ Area%$^\blacklozenge$	4.1	4.1	1.6	6.9	9.9	7.9	0.0	1.4
Density(g/cm^3)	5.2$^\blacklozenge$	5.1$^\blacklozenge$	3.8	3.8	3.3	3.3	2.7	2.7

†The Cr-content of C$_2$S is based on EPMA due to a sum-peak Si+Ca interference in EDX.

*Total Fe is expressed as Fe$_2$O$_3$.

$^\blacklozenge$1σ standard deviation on the area% for the 9 individual fields measured.

$^\blacklozenge$Densities calculated using crystal density and wt% of Fe-Wüstite, Mg- Wüstite and Magnetite from Rietveld analysis.

because EDX analysis is not suitable for detecting CO$_2$ vs·H$_2$O groups in phases. Therefore, it is unclear if the phase is f-lime, calcite, or portlandite. According to the Rietveld quantification, only small amounts of CaO were present in the starting materials of S-58 and S-16.

S-58 and S-16 are derived from the same BOF slag lot, although their amounts of brownmillerite and C$_2$S (β-C$_2$S + α'-C$_2$S) differ by 6.6 area%, while the MgFeOx (Wüstite + Magnetite) area% of both samples are similar. Nevertheless, the phase amounts for the non-hydrated samples S-16 and S-58 agree with the variance (σ Area% in Table 3) observed for the 9 measured fields. Furthermore, as expected, the equivalent phases in S-58 and S-16 demonstrated good correspondence in chemical composition, because the PARC compositions are derived from the sum

spectrum of all pixels in the spectral image identified as belonging to the same phase.

Because the BOF slag samples are obtained from many BOF process batches, each grain can come from a different batch. Consequently, some variance in the composition of the phases in the measurement area is expected. PARC can also detect trace elements in the phases, so it is possible to identify the phases that contain chromium (Cr) and vanadium (V). The results in Table 4 reveal that chromium is found mainly in wüstite and brownmillerite, whereas vanadium is primarily found in C$_2$S and brownmillerite.

Table 4

Phase proportions from different methods and their correspondence to the measured bulk composition for S-16 and S-58. LSQ =least square method.

Sample		S-16			S-58		
Phase (wt%)		PARC*	LSQ phase	QXRD	PARC*	LSQ phase	QXRD
Wüstite + Magnetite		30.5	31.5	32.9	30.0	32.4	27.8
Brownmillerite		19.4	22.4	17.2	25.8	17.9	16.3
β-C$_2$S + α'-C$_2$S		50.1	46.0	33.0	44.2	46.4	40.4
f-lime + Portlandite +Calcite		0.0	0.1	0.6	0.0	3.4	0.6
Amorphous				16.4			14.8
Oxide (wt%)	XRF (Table 1)	PARC	LSQ bulk		PARC	LSQ bulk	
Na$_2$O	0.0	0.1	0.1		0.0	0.0	
MgO	8.0	8.1	8.3		7.7	8.2	
Al$_2$O$_3$	2.3	2.5	2.8		3.3	2.4	
SiO$_2$	13.4	14.6	13.5		13.1	13.5	
P$_2$O$_5$	1.6	1.7	1.5		1.6	1.6	
SO$_3$	0.0	0.1	0.1		0.1	0.1	
Cl	0.0	0.0	0.0		0.0	0.0	
K$_2$O	0.0	0.0	0.0		0.0	0.0	
CaO	38.0	39.3	38.1		37.9	38.7	
TiO$_2$	1.4	1.6	1.8		1.6	1.3	
V$_2$O$_5$	1.0	0.9	0.9		0.9	0.8	
Cr$_2$O$_3$	0.3	0.2	0.3		0.2	0.2	
MnO	4.2	4.1	4.2		3.8	4.1	
Fe$_2$O$_3$	28.0	26.5	28.0		29.4	28.6	
Total	98.2	99.7	99.7		99.7	99.7	
Sum of squares of deviation		5.6	0.5		3.7	1.0	

* PARC phase amounts were converted from area% (Table 3) to weight% using the corresponding Rietveld crystal phase densities (Table 2).

3.1.3. Internal consistency of analytical methods using XRD, XRF, and PARC

The PARC chemical compositions of MgFeOx, C_2S, Brownmillerite, and CaO /Ca(OH)$_2$/ CaCO$_3$ (Table 3) were used to fit the XRF bulk composition with a least square method (LSQ) mass balance to access the amount of each phase in wt%. According to the established boundary conditions, each phase had to contribute, and the sum of all phases had to be 100%. The fitted bulk composition based on LSQ is given in Table 4 and compared to the bulk composition as determined by XRF and with PARC. The PARC bulk composition was calculated using the PARC chemical composition of each phase (Table 3), and the PARC phase amounts in wt% (Table 4), calculated using crystal density from each phase given in Topas. The consistency of LSQ vs. PARC with the XRF measurement can be seen in the sum of squares of deviation.

Furthermore, the phase amounts acquired from the LSQ fit were compared to those measured using XRD and PARC. For the comparison, magnetite and wüstite detected by XRD were summed up and compared with the PARC phase MgFeOx. C_2S is the sum of α`-C_2S and β-C_2S from XRD. The values from PARC and XRD agree for MgFeOx and brownmillerite. However, the amount of C_2S detected by PARC was much higher than that detected by XRD for both S-16 and S-58. This difference is attributed to the capacity of PARC to detect amorphous content as well. These results imply that part of the C_2S is amorphous [22] and becomes amorphous during milling. Sample S-16 contained a more amorphous phase and less C_2S in the QXRD results because it was milled longer. The amorphous phase increased during milling, and C_2S presents a higher degree of amorphization than the other phases. This effect is linked to the specific fracture energy, cooling process, and stress generation [16,31,53].

The bulk composition determined using LSQ was in close agreement with the composition measured by XRF. However, the bulk composition derived with PARC slightly deviates, as is apparent from the higher sum of squares of deviation (Table 4), which suggests that phase proportions from PARC are less reliable for the sample scan from an area of 1.5×1.2 mm^2 (3×3 fields), as expected, based on the standard deviation shown in Table 3. Therefore, to continue the investigation and gain more reliable values, 7×7 fields were analyzed for the hydrated samples.

3.2. Hydration of BOF slag

3.2.1. Isothermal calorimetry

Samples S-58 and S-16 were mixed with water (w/s = 0.4) to assess the heat release of BOF slag during 90 h of hydration (Fig. 3). S-16 presented the highest cumulative heat release after the first 48 h with 74.8 J/g and 31 J/g for S-58. Samples with smaller particle sizes present a larger specific surface area (SSA=0.5 m^2/g). As expected, S-16 released more heat than S-58 (SSA=1.5 m^2/g). The specific surface area was not the only factor that influenced the reactivity. Intensive milling can cause mechanical activation of phases, making them more reactive [31]. Although the mineralogy of the two samples was essentially the same because they came from the same lot, their difference in reactivity can be found in the hydration products. The mineralogy of hydrated BOF slag was studied to investigate the reactive phases contributing to the higher heat release in S-16 than in S-58.

3.2.2. Mineralogy of hydrated BOF slag

3.2.2.1. Quantitative X-Ray diffraction (QXRD) analysis. The reaction products of BOF slag (w/s = 0.4) were measured with XRD and quantified (Table 2) after 7, 14, 21, 28, 56, and 90 days of hydration and compared to the starting material (0d). The Rietveld analysis showed that the following crystalline reaction products were present in small amounts after hydration in both S-58 and S-16: portlandite, pyroaurite [Mg$_6$Fe$_3$(CO$_3$)(OH)$_{16}$·4(H$_2$O)] and Fe-katoite [(Ca$_3$Fe$_2^{3+}$(OH)$_{12}$]. The
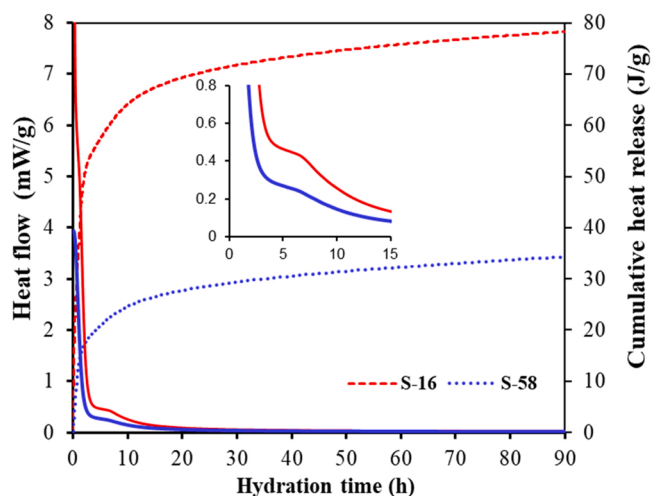

Fig. 3. Rate of heat flow and cumulative heat release of S-16 and S-58. Color should be used in print.

latter two phases represent the Fe-member of the hydrotalcite series [54, 55] and the Fe-containing hydrogarnets, respectively [56]. Both Al and Fe occupy trivalent cation positions in the crystalline phases pyroaurite and Fe-katoite, resulting in an uncertain exact Fe/Al ratio. For Fe-katoite, an arbitrary Al:Fe ratio of 3:1 in the crystal structure was adopted for Rietveld refinement. Hydrogarnets also have variable Si contents. The solid solution end-members were katoite (C$_3$(A,F)H$_6$) and hibschite (C$_3$(A,F)S$_2$H$_2$). Although it was not possible to determine the Si site occupancy ascribable to the low crystallinity of the hydration product, so the Fe-Katoite composition was used for all refinements.

With the mineralogical composition from Table 2, the graphs in Fig. 4a and b present the change in the phase proportion over time. The hydrated samples contained two types of amorphous phases: the amorphous material achieved by milling, as seen in the non-hydrated samples, and the amorphous reaction products in the hydrated samples. The amorphous content in unreacted BOF slag is expected to be more reactive than the crystalline phases. Therefore, the amorphous content was consumed first, decreasing its content by forming Fe-katoite and Pyroaurite. Further hydration increased the amorphous content on account of the formation of amorphous reaction products. S-58 was subjected to less milling amorphization, and its crystalline reactants were consumed earlier, as seen in the C_2S-polymorphs from 7 days (versus at 14–21 days in S-16). In S-16, the drop in the C_2S content was steeper (higher rate of change). However, based on the XRD results alone, it is not possible to identify the nature of the hydrated amorphous component nor distinguish it from the possibly remaining anhydrous amorphous component.

The heat evolution measured by calorimetry (Fig. 3) is largely attributed to the reaction of brownmillerite, which was consumed at an early age. Its rate of change was the same in S-16 and S-58 for up to 90 days (Fig. 4), but a higher amount of hydrogarnets was formed after 7 days in S-16 than in S-58, which could explain the differences observed in calorimetry [57]. However, after 7 days, the hydrogarnet formation rates were very similar.

After 14 days, the hydration activity forming crystalline hydrogarnet reached a plateau in both samples (Table 2). Meanwhile, the amorphous content kept rising continuously and was still increasing at 90 days, the end of the observed time series. Alongside, portlandite increased while pyroaurite decreased in both samples. S-16 developed more amorphous and crystalline hydration products than the S-58, indicating that the longer-milled smaller particle size promotes hydration over time.

The crystalline Fe-bearing phase wüstite partakes in the reaction of S-58 after 21 days, whereas in S-16, it is consumed continuously. The wüstite content in S-58 and S-16 decreased by approximately 33% and
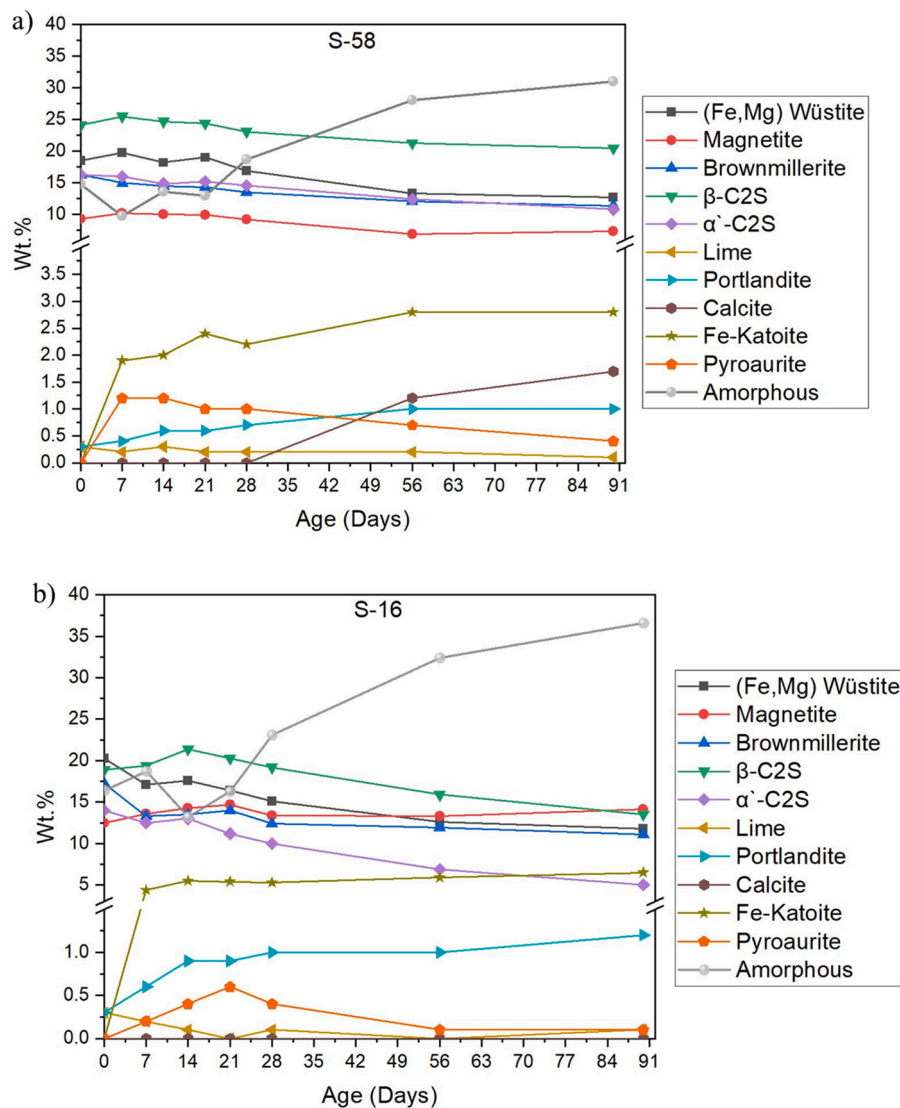
Fig. 4. Phase proportions of hydration of BOF slag over time for S-58 and S-16 determined by XRD (data from Table 2). Color should be used in print.

42%, respectively, in relation to the starting proportions until the 90-day observation period. The reactivity of wüstite with water in BOF slag is a novel observation that has not been previously described in the literature. Instead, publications have suggested that wüstite is an inert phase [33,58–61] that only partially reacts under autoclaving conditions [62]. Additionally, magnetite appeared to be an inert phase; it did not react in either sample. Regarding other minor crystalline hydration products, S-58 formed more pyroaurite, while S-16 formed more portlandite.

The crystalline C_2S phases did not appear to react in the first 14 days of hydration. In contrast, their amorphous counterparts were consumed, as corroborated by the early decrease in the amorphous content. Subsequently, the C_2S phases started partaking in the hydration reaction and were reduced by 20–25% after 90 days, even more so in S-16, with 33% of α'-C_2S being consumed compared to the starting amount. As in OPC, the polymorph α'-C_2S also appears to be more reactive than β-C_2S for BOF slag. [63]. However, it is important to mention that low levels of amorphous content (0–15 wt%) are difficult to determine with the Rietveld method using the internal standard approach [27].

3.2.2.2. Scanning electron microscopy (SEM) and PARC. Fig. 5(a and b) presents S-58 and S-16 after 21 days of hydration in an SEM back-scatter image, while Figs. 6 and 7(c and d) show the PARC phase maps of the same samples. The black (pixels) area is referred to as the resin

embedding and is not included in the phase fraction calculations. After hydration, a new phase was detected by PARC with a distinct chemical composition called "Hydration products". The phase proportions and compositions are presented in Table 5. As expected, the unreacted primary minerals had nearly identical compositions in the two hydrated samples compared to the non-hydrated samples. The hydration product in S-58 21d represents 15.2% of the area, accounting for 28.8% in S-16 21d. The amount of the f-lime + Portlandite + Calcite phase has also increased. Although PARC cannot directly confirm that this occurred because of the formation of portlandite. The composition of portlandite was remarkably similar in S-58 and S-16, and very different from that of the original free-lime phase, which was much Mn- and Fe-richer, as identified with PARC in non-hydrated S-58. XRD and DTG also confirm the presence of portlandite in these samples.

The deviation of around 15–20% relative to each phase amount determined with PARC (σ Area% in Tables 4 and 6) is the same for 9 or 49 fields analyzed, supporting the earlier inference that phase proportions measured with PARC demonstrate a large variation per SEM image field (0.5 ×04). This deviation is unavoidable when using this imaging method, although it does not influence the reliability of the chemical composition determined by PARC.

Overall, S-16 shows more reaction than S-58 with 35 area% vs. 20 area% of products when including portlandite {Ca} with the "Hydration
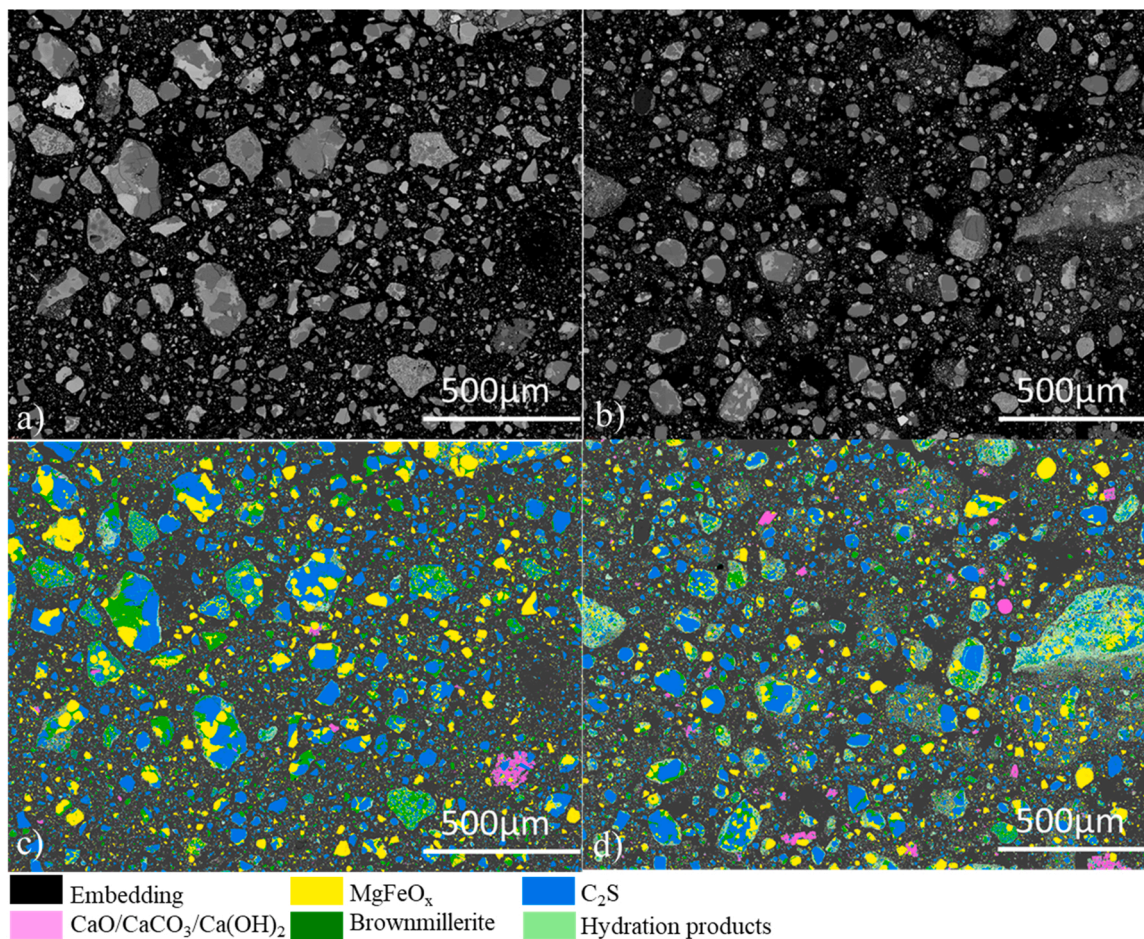
Fig. 5. SEM BSE picture and PARC phase map of S-58 21d (a and c) and S-16 21d (b and d). Color should be used in print.
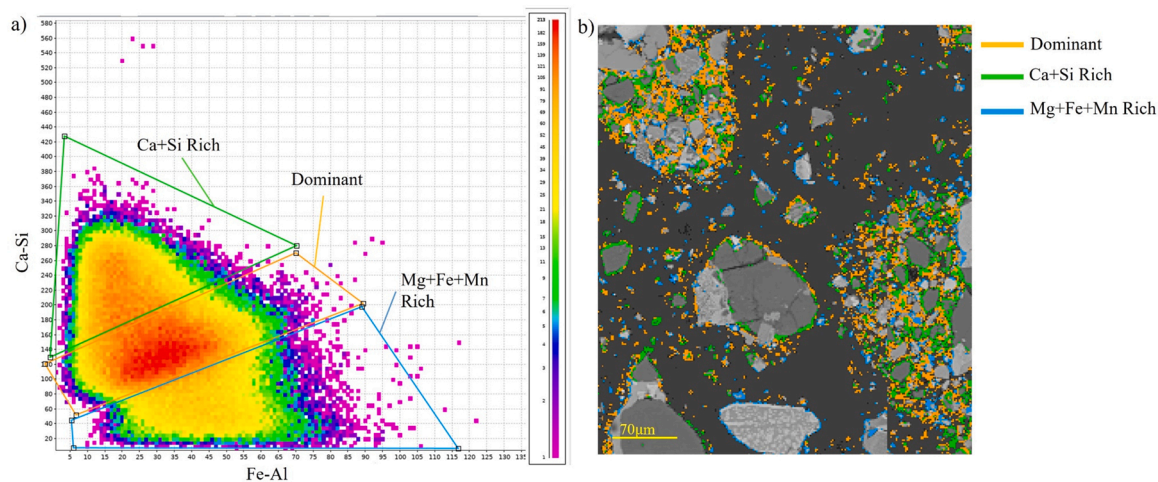

Fig. 6. a) The intensity of the Fe+Al Kα peak is plotted against the intensity of Ca+Si Kα for all pixels belonging to the "Hydration products" phase that was determined with PARC (Sample S-16 21d). The color indicates the density of overlapping data points. The pixels are also divided into three subareas (Dominant, Ca+Si rich, and Mg+Fe+Mg rich; b) SEM BSE image with the "Hydration products" phase in S-16 21d marked in colors corresponding to the area selected in the density plot (the units are EDX channel counts). Color should be used in print.

products". The higher amount of hydration products in S-16 at 21d confirms the calorimetry and XRD results. The hydration product composition differs between S-16 and S-58, with the latter being much richer in the Ca-silicate component and poorer in FeO. The minor elements in the "Hydration products" phase are MgO, Al_2O_3, MnO, P_2O_5,

V_2O_5 and TiO_2. The presence of Al_2O_3 and TiO_2 indicates that the brownmillerite contributed to the hydration product. The MgO and MnO imply the reaction of wüstite, while the SiO_2 and P_2O_5 are contributed by the reaction of α'-C_2S and β-C_2S.

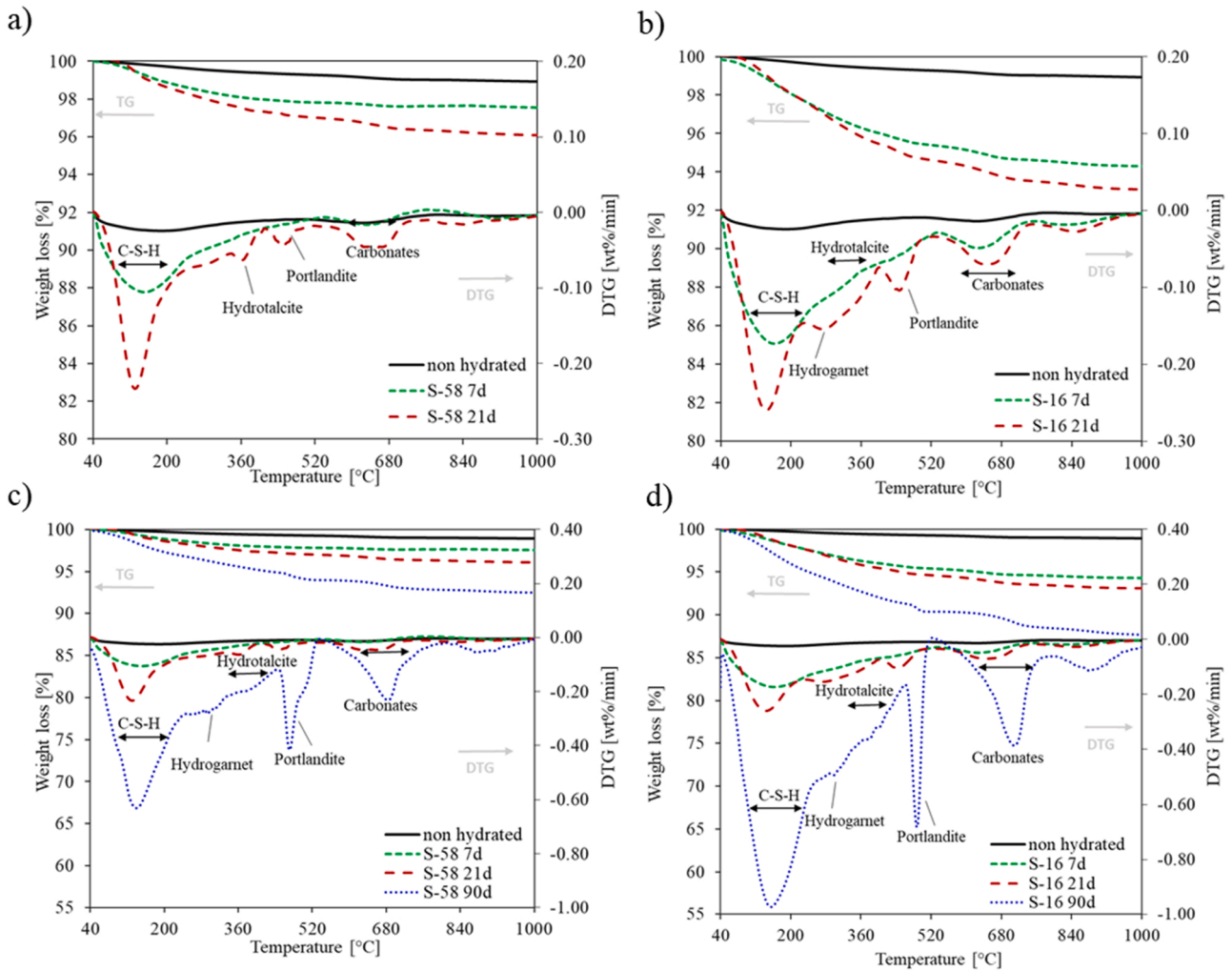The "Hydration products" phase is not homogeneous; rather, it has a

Fig. 7. TGA and DTG of the non-hydrated sample and samples after 7 and 21 days of hydration for (a)S-58 and (b) S-16, (c) and (d)after 90 days, respectively. Note: BOF slag non-hydrated S-58 and S-16 present the same curve.

Table 5
The average chemical composition (sum spectrum) and amount (area%) of phases after 21 days of hydration, as identified in S-16 21d and S-58 21d with PARC.

Compound concentration wt%	{Mg, Fe}		{Ca, Fe}		{Ca, Si}		{Ca}		{Ca, Si, Fe}	
	Wüstite +Magnetite		Brownmillerite		β-C$_2$S + α'-C$_2$S		f-lime + Portlandite+Calcite		Hydration product	
	S-16 21d	S-58 21d	S-16 21d	S-58 21d	S-16 21d	S-58 21d	S-16 21d	S-58 21d	S-16 21d	S-58 21d
Na$_2$O	0.0	0.0	0.2	0.2	0.1	0.1	0.0	0.1	0.0	0.4
MgO	26.0	24.5	0.8	0.6	0.2	0.2	0.3	0.3	5.4	3.5
Al$_2$O$_3$	0.2	0.2	10.4	10.7	0.6	0.6	0.3	0.3	2.8	2.0
SiO$_2$	0.5	0.5	2.1	2.1	29.0	28.7	0.9	1.0	17.0	22.2
P$_2$O$_5$	0.0	0.0	0.2	0.2	3.3	3.3	0.3	0.3	1.9	2.5
SO$_3$	0.0	0.0	0.1	0.1	0.2	0.2	0.2	0.2	0.2	0.3
Cl	0.0	0.0	0.0	0.0	0.0	0.0	0.0	0.0	0.1	0.1
K$_2$O	0.0	0.0	0.0	0.0	0.0	0.0	0.1	0.1	0.0	0.0
CaO	1.9	2.2	42.4	42.1	61.8	61.9	94.9	93.7	42.4	47.3
TiO$_2$	0.0	0.0	5.4	4.4	1.0	1.0	0.6	0.6	1.7	1.5
V$_2$O$_5$	0.1	0.1	1.5	1.4	1.1	1.1	0.1	0.1	1.2	1.3
Cr$_2$O$_3$ †	0.6	0.5	0.3	0.2	0.1	0.1	0.0	0.0	0.4	0.4
MnO	11.9	11.1	1.3	1.4	0.0	0.1	0.5	0.9	3.5	2.9
Fe$_2$O$_3$*	58.7	60.9	35.3	36.7	1.7	1.9	1.9	2.4	23.4	15.5
Amount Area%	18.4	23.0	12.8	17.9	33.4	39.4	6.6	4.4	28.8	15.2
σ Area%♣	2.3	3.3	1.1	2.8	6.2	5.8	1.1	1.4	3.0	1.4
Density(g/cm^3)	5.2♦	5.1♦	3.8	3.8	3.3	3.3	2.8	2.7	2.4✦	2.1✦

†The Cr-content of C$_2$S is based on EPMA due to a sum of the peaks Si+Ca interference that occurs in EDX.

*Total Fe is expressed as Fe$_2$O$_3$.

♣1σ standard deviation on the area% for the 49 individual fields measured.

♦densities calculated using crystal density and wt% of Fe-Wüstite, Mg- Wüstite and Magnetite from Rietveld analysis.

✦calculated using sample density, the phases crystal density and PARC area%.

Table 6

Composition of the plot of the three subareas (Dominant, Fe+Mg+Mn rich, and Ca+Si rich) obtained from the "Hydration products" phase in S16–21d.

Areas	Na$_2$O	MgO	Al$_2$O$_3$	SiO$_2$	P$_2$O$_5$	SO$_3$	K$_2$O	CaO	TiO$_2$	V$_2$O$_5$	Cr$_2$O$_3$	MnO	Fe$_2$O$_3$
Hydration product	0.1	5.4	2.8	17.0	1.9	0.2	0.0	42.4	1.7	1.2	0.4	3.5	23.4
Dominant	0.0	4.9	3.6	15.8	1.7	0.3	0.0	42.0	2.1	1.4	0.4	3.2	24.7
Fe+Mg+Mn rich	0.1	14.7	2.6	6.9	0.6	0.2	0.0	17.3	0.7	0.7	0.4	8.1	47.8
Ca+Si rich	0.1	2.3	1.6	24.2	2.9	0.3	0.0	54.4	1.3	1.3	0.5	1.4	9.6

relatively wide, continuous composition range. To indicate its compositional variation, the combined Ca+Si EDX spectra peak intensities were plotted against that of the Al+Fe peaks for every pixel belonging to the "Hydration products" (Fig. 6a). The compositional range was separated into three subregions to determine the presence of calcium silicates and Al/Fe oxides. The pixels belonging to each subregion are shown in the SEM image (Fig. 6b). There is a Dominant area similar to the original "Hydration products" composition, a small area that is more Ca+Si rich and a second minor area rich in Mg+Fe+Mn, which is more likely to be hydrated areas of wüstite.

The "Hydration products" phase represents a mixture of the amorphous and crystalline phases (the latter visible in XRD), which cannot be distinguished further, as individual phases, regarding the limit of the EDX resolution of around 1 μm for the conditions of the spectral acquisition. The dominant composition (Table 6) of the hydration products was similar to the bulk hydration product. The deviant compositions were influenced by either a higher C$_2$S or a higher wüstite contribution.

The phase proportions (in wt%) of the "Hydration product", {Ca}Portlandite, and the unreacted phases based on the PARC measurements are presented in Table 7. The phase amounts were calculated from the area to wt% using the densities in Table 5. The densities of the crystalline phases were taken from the Rietveld refinement results. The true density of the newly formed "Hydration product" is unknown. Its density was derived from the difference between the overall sample density measured using a He-pycnometer and the known crystal densities (Table 2). The derived densities for the "Hydration product" are 2.4 g/cm^3 for S-16 21d and 2.1 g/cm^3 for the S-58 21d sample (Table 5) based

on sample densities of 3.4 and 3.6 g/cm^3. This density difference is also reflected in the compositional variance of the "Hydration product" between the samples, S-58 21d being relatively Ca-Si rich and S-16 21d, Ferich.

The content of the product phases, Portlandite + "Hydration product", was 25.4 wt% and 12.1 wt% for S-16 21d and S-58 21d, respectively. It should be emphasized that the "Hydration products" area, as observed with SEM, includes all porosity that is beyond the Spectral Imaging spatial resolution (< ~1-micron porosity). The spatial resolution of EDX is also too low to detect hydrogarnet and hydrotalcite separately, as observed with XRD.

3.2.2.3. Internal consistency of analytical methods using XRD, XRF, and PARC. Similarly, as the phase proportions were calculated for the unreacted BOF slag samples (Table 4), LSQ fit mass balance calculations were also conducted for the hydrated samples, as shown in Table 7. As the bulk composition of the hydrated samples was the same as that of the unreacted samples, except for the addition of water, it was possible to fit the original slag phases in Table 3 to the bulk composition. This yielded the initial phase amounts for the unreacted slag again, as shown in the *LSQ phase*. The derived phase proportions are similar to those from PARC and LSQ-phase for the unreacted slag.

The composition of the "Hydration product" was also fitted using the least square method (LSQ). It was assumed that each of the original slag phases hydrates and contributes to the composition of the "Hydration product". Therefore, its composition was fitted using the PARC phase composition of each unreacted phase from Table 5. The results, given under the entry *LSQ rx* in Table 7, demonstrate how much of each

Table 7

PARC and QXRD measured phase amounts and LSQ mass balances observations for S-16 21d and S-58 21d. The LSQ phase with reference to XRF (Table 1) and LSQ rx phase amounts reacting to form the PARC composition of the hydration product. All data are in wt%.

Sample		S-16 21d				S-58 21d			
Phases (wt%)		QXRD	LSQ phase	PARC	LSQ rx	QXRD	LSQ phase	PARC	LSQ rx
Wüstite + magnetite		31.1	*31.8*	27.8	*4.8*	28.9	*33.1*	32.8	*1.6*
Brownmillerite		14.0	*24.0*	14.3	*4.5*	14.3	*20.2*	18.9	*0.6*
β-C$_2$S + α'-C$_2$S		31.6	*44.2*	32.5	*10.6*	39.6	*46.1*	36.2	*6.3*
f-lime + Portlandite + Calcite		1.1	-	5.4	*0.0*	0.8	*0.7*	3.3	*0.0*
Hydration product		5.9	-	}20.0	}20.0	3.4	-	}8.8	}8.8
Amorphous		16.3				13.0			
Hydration product phase composition				PARC	LSQ bulk			PARC	LSQ bulk
Oxide (wt%)									
Na$_2$O				0.0	*0.1*			0.4	*0.1*
MgO				5.4	*5.9*			3.5	*3.9*
Al$_2$O$_3$				2.8	*3.2*			2.0	*2.0*
SiO$_2$				17.0	*16.8*			22.2	*22.3*
P$_2$O$_5$				1.9	*1.9*			2.5	*2.6*
SO$_3$				0.2	*0.1*			0.3	*0.1*
Cl				0.1	*0.0*			0.1	*0.0*
K$_2$O				0.0	*0.0*			0.0	*0.0*
CaO				42.4	*42.2*			47.3	*47.3*
TiO$_2$				1.7	*2.0*			1.5	*1.4*
V$_2$O$_5$				1.2	*1.0*			1.3	*1.0*
Cr$_2$O$_3$				0.4	*0.2*			0.4	*0.1*
MnO				3.5	*2.9*			2.9	*1.8*
Fe$_2$O$_3$				23.4	*23.1*			15.5	*15.6*
Total				100.0	*99.6*			100.0	*98.2*
Sum of squares of deviation	with reference to the bulk composition		0.7	7.1			0.7	1.9	
	with reference to PARC hydration product				1.1				1.5
Degree of hydration (DOH)				29%				15%	

original slag phase has reacted and contributed to the composition of the hydration product. The degree of hydration (DOH) was also calculated for the hydrated samples after 21d using EDX mappings from SEM, according to Kocaba et al. [42]. Sample S-58 21d presented a DOH of 15%, and S-16 21d reached a DOH of 29%.

The reactant proportions in wt% in S-16 after 21d are roughly Wu: C_2F: C_2S = 1:1:2, and in S-58 after 21d are Wu: C_2F: C_2S= 1:1:5. Overall, the C_2S-polymorphs are the predominantly reacting phases, contributing approximately 50% and 70% to the hydration product in S-16–21d and S-58–21d, respectively. Details of the calculations are provided in Appendix B.

As was done for the non-hydrated samples, the phase amounts for the 21d samples can be compared between PARC and the XRD-Rietveld analysis. The comparison shows that most phases are reasonably close, with a maximum deviation of 4.6 wt% absolute on any phase groupings. What stands out is the much lower portlandite content in QXRD than that in PARC.

The much higher amounts of C_2S-polymorphs detected with PARC in the non-hydrated slag, compared to QXRD, seem to have disappeared during hydration, indicating that amorphous C_2S preferentially contributed to the formation of the hydration products, which was further supported by the high amount of C_2S consumed to form the reaction product, as calculated by the LSQrx fit (Table 7). The LSQrx fit yielded low portlandite contents similar to the QXRD, contrary to the higher content observed with PARC.

The crystalline hydration products from XRD, hydrogarnets, and pyroaurite, unlike portlandite and calcite, do not have an equivalent PARC phase, as mentioned previously. Therefore, the crystalline hydration products hydrogarnet and pyroaurite must be located in the PARC hydration product, together with amorphous product phases.

3.3. Thermogravimetric analysis

Thermogravimetric analysis (TGA) and its differential thermogravimetric analysis (DTG) were used to determine the content of portlandite and calcite, as well as the water content of the other hydration phases [38]. The TGA/DTG curves for S-58 and S-16 after 7, 21 (Fig. 7a-b), and 90 days (Fig. 7c-d) demonstrate characteristic peaks that rise with hydration time and with SSA increase. For the non-hydrated sample, the total weight loss value was 0.92 wt%. The weight loss for S-58 after 7 and 21 days of hydration was 2.33 wt% and 4.33 wt%, respectively, reaching 7.39% at 90d. For S-16, after 7 and 21 days of hydration, the weight loss was 4.13 wt% and 6.31 wt%, respectively. After 90 days, sample S-16 reached 11.36% of weight loss.

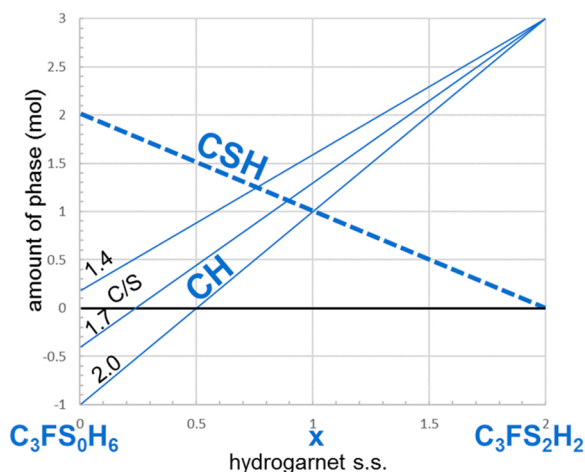The volatiles present in the samples were quantified by TGA and,

Fig. 8. Change of silica in the solid solution series of katoite-hibschite parameters in the hydrogarnet formation. C/S refers to the C-S-H phase (Eq. (3)).

based on the mass release over temperature, assigned to water and CO_2 in the corresponding phases.

In terms of weight loss attributed to specific phases, the TGA can be separated into the following temperature ranges: (i) 40–400 °C, weight loss is associated with decomposition of amorphous hydration products [38], including dehydration of hydrogarnets [56] and pyroaurite [64]; (ii) between 400 °C and 500 °C, associated with the dehydration of Ca (OH)$_2$ and (iii) between 530 °C and 750 °C attributed to volatilization of CO_2 after the decomposition of carbonates. The peak around 850 °C is related to the effect of the organic solvent (isopropanol) used to stop the hydration reaction of the sample [65]. Hydrotalcite, generally, presents characteristic mass-loss in three regions, 25–65 °C adsorbed water, up to 200 °C intercalated water, from 300 °C to 400 °C interlayer-hydroxyl water, and CO_2 [64] with the dihydroxylation shifting to lower temperatures with increasing iron content for pyroaurite [54], observed in the 90 days samples with the broadening of the peaks associated with C-S-H and hydrogarnet.

The DTG does not present peaks of portlandite for the samples at 7 days, although there is a mass loss in the corresponding range associated with the phase, and small amounts of portlandite were observed with XRD at the same age. Broad peaks of C-S-H can be observed with overlapping mass losses up to 300 °C associated with hydrogarnet and pyroaurite for both samples [56]. After 90 days of BOF slag hydration, the DTG peaks can confirm the evidence of the phases formed, not only being more intense for S-16 than S-58, but also presenting differences in phase proportions.

Table 8 shows the equivalent amounts of portlandite (Ca(OH)$_2$) and calcite (CaCO$_3$) calculated for the weight loss values, as well as the observed amount of portlandite quantified with XRD and the {Ca}-phase from PARC. TGA is more sensitive than XRD in detecting low amounts of portlandite and carbonates [38]. It is important to mention that no crystalline carbonate-bearing phases other than pyroaurite were detected in the XRD quantification of the TGA data samples.

Table 9 lists the H_2O- and CO_2-loss associated with the crystalline phases' decomposition. It is based on the amounts of each phase detected with QXRD, subtracted from the total volatiles measured with TGA and used to determine the volatile content of the amorphous reaction products. It is well known that before and during the curing, some of the portlandite reacts to carbonate with the inevitable exposure to CO_2 in the air [66–68]. Therefore, TGA indicates the decomposition of small amounts of carbonates that are not visible in XRD [69], though, in the longer cured samples of S-58 (56 and 90 days), calcite was indeed found with XRD. It should be emphasized that the high-temperature mass loss attributable to decarbonation partially results from the decomposition of pyroaurite, which contains CO_2. However, as shown in Table 9, the released amount of CO_2 is very small.

Table 8 and Table 9 show that the crystalline phases only account for a small fraction of the volatiles found in TGA, and approximately two-thirds of the H_2O and over 90% of the CO_2, appear to be incorporated into the amorphous reaction products, or possibly only adsorbed to the surface. In addition, the PARC measurements already provide evidence for the presence of more {Ca} phase (lime/hydrate/carbonate) than that found in QXRD, thus indicating that the Ca-hydrate/carbonate phases are in amorphous form.

Each of the techniques mentioned above yields specific information with its limitations. PARC analysis provided spatial distributions of compositions without volatiles, as they were not measurable with EDX. XRD could identify the crystalline hydration phases, but not the amorphous constituents. TGA is limited because it provides the mass of total volatiles, which can only be cautiously attributed to decomposing phases and their known H_2O or CO_2 content.

3.4. Assessment of PARC "Hydration product"

After hydration, a new PARC group with an identified compositional range was observed in the BOF slag, as shown in Fig. 5. The identified

Table 8

Weight loss for each sample, related to the type of volatile and decomposing phase based on TGA, in comparison to XRD and PARC, in wt%.

Sample	Phases							
	Weight loss (TGA)			Calculated (TGA)		Measured		
				-	-	XRD	PARC	
	40 ℃ − 400 ℃ Amorphous C-S-H, Hydrogarnet, Pyroaurite	400 ℃ − 500 ℃ Ca(OH)$_2$	500 ℃− 750 ℃ Amorphous carbonates, CaCO$_3$, Pyroaurite	CaCO$_3$	Ca(OH)$_2$	- Ca(OH)$_2$	- {Ca}	
Non-hydrated	-	-		-	-	0.27	0.04	
S-58 7d	1.99	0.16	0.18	0.48	0.80	0.44	-	
S-16 7d	2.87	0.58	0.68	0.97	2.03	0.63	-	
S-58 21d	2.77	0.90	0.66	1.50	3.00	0.59	3.30	
S-16 21d	4.61	0.73	0.97	2.21	3.69	0.91	5.43	
S-58 90d	4.99	0.92	1.48	3.36	3.78	0.98	-	
S-16 90d	8.53	0.98	1.85	4.20	4.03	1.19	-	

Table 9

Volatile content in crystalline phases (XRD) and amorphous phases based on TGA in the hydration products of S-58 and S-16 after 7, 21, and 90 days, in wt%.

Sample	Bound H$_2$O					CO$_2$ content			
	Total	Portlandite	Pyroaurite	Hydrogarnet	Amorphous	Total	Calcite	Pyroaurite	Amorphous
S-58 7d	2.15	0.11	0.37	0.49	1.18	0.18	0	0.07	0.11
S-16 7d	3.45	0.15	0.05	1.11	2.13	0.68	0	0.01	0.67
S-58 21d	3.67	0.14	0.29	0.61	2.63	0.66	0	0.06	0.60
S-16 21d	5.34	0.22	0.15	1.37	3.6	0.97	0	0.03	0.94
S-58 90d	5.91	0.24	0.13	0.72	4.82	1.48	0.74	0.01	0.72
S-16 90d	9.51	0.29	0.03	1.64	7.55	1.85	0	0.03	1.84

PARC reaction product represents a mixture of crystalline and amorphous phases, which is too small to be resolved by EDX. The portlandite phase appears to form spatially separated from a C-S-H, as in hydrated Portland cement.

Kaja et al. [22] suggested that the PARC reaction product of BOF slag hydration is a combination of hydrotalcite, hydrogarnet, and C-S-H gel phases, either in the crystalline or amorphous state. Their postulated phase assemblage for the hydration product in the presence of portlandite is supported by the QXRD data of the present work, in which the hypothesis is further analyzed by performing an LSQ fit to match the chemical composition of the PARC reaction product to a sum of hydrotalcite, hydrogarnet, and C-S-H gel. The following arguments can be made to support the choice of these three phases. The hydrotalcite in the hydration product is expected to host the di-valent cations [70]. Hydrotalcite-pyroaurite solid solution phases $M_6(A,F)cH_{12}$ are poorly crystalline when formed at room temperature [71]. The M/(A,F) ratio is reported to vary between 3.8 and 8.7 [72]. In the LSQ fit, the composition of the hydrotalcite was assumed to accommodate all divalent cations, and a ratio of M/(A,F)= 6 was adopted for the calculation. The presence of hydrogarnet is supported by Dilnesa et al. [55] and Vespa et al. [73] studies on hydrogarnet stability in Fe-containing cement systems. Because hydrogarnets have a variable composition, two end-member compositions, katoite $C_3(A,F)H_6$ and hibschite $C_3(A,F)S_2H_2$, were used for the calculation. Literature [74,75] has indicated that when portlandite is present in the system, the C-S-H gel has a variable C/S ratio above ~1.4–1.5, in which values close to 1.67–2.0 were found. The C/S ratio was fixed at 1.7 to make LSQ calculations. Some trivalent cation presences (Fe^{3+}, Al^{3+}) in the C-S-H phase can occur but have not been allowed in our calculation. This seems justifiable based on the low alumina content of BOF-slag ($Al_2O_3 < 2$w.t.%) and the presence of hydrogarnet and hydrotalcite accommodating the trivalent cations. Mancini et al. [76] indicated that the equilibrium uptake in C-S-H is very low because of the low solubility of Fe^{3+} in the slag pore solution. Furthermore, for the calculations, it was assumed that substitution rules (Goldschmidt rules) [77] apply to cations with comparable valency and ionic radii. Consequently, the cations Si^{4+}, P^{5+}, V^{4+}(or V^{5+}), and Ti^{4+} ($\Sigma M^{4+,5+}$) are considered interchangeable and can occupy the same atomic position in a crystal lattice. The same holds for Al^{3+}, Fe^{3+}, Cr^{3+}

(ΣM^{3+}) and Mg^{2+}, Fe^{2+}, Mn^{2+} (ΣM^{2+}), and lastly Ca^{2+}, Na^+ and K^+ ($\Sigma M^{2+,1+}$). We will refer to these as valency groups (ΣM). Based on its composition, hydrotalcite contains the valency groups ΣM^{3+} and ΣM^{2+}. For Fe-katoite it is ΣM^{3+} and $\Sigma M^{2+,1+}$, for hibschite $\Sigma M^{4+,5+}$, ΣM^{3+} and $\Sigma M^{2+,1+}$ and for C-S-H it is $\Sigma M^{4+,5+}$ and $\Sigma M^{2+,1+}$. Some ions have a preference for specific hydration phases, however, there is insufficient information available to quantify this behavior. Therefore, ions were evenly distributed in each valence group to perform the calculations. In the calculated molar mass balance of the hydration phases in the "hydration product" PARC phase (Appendix B - "*norm calc*" sheets), any redistribution of exchangeable cations is in theory possible and does not affect the outcome of phase proportions, i.e., the molar fractions of hydrations phases are independent of the (unknown) effective cation distribution.

The extent to which the oxidation of the Fe^{2+} in wüstite occurs in the hydration reactions was unknown. However, it was considered that all divalent iron provided by the reacting {Mg, Fe} phase oxidized to a trivalent state during hydration. The outcomes are presented in Table 10 for sample S-16 21d. Further details about the calculation itself and the results for sample S-58 21d can be found in Appendix B ("*norm calc S-16 3$^+$*" and "*norm calc S-58 3$^+$*").

Table 10 shows the phase stoichiometry of the reaction products used in the calculations to fit the reaction products to the overall PARC hydration products.

From this sample S16–21d calculation, only a small amount of water was over-allocated (calculated 4.7 wt% vs. TGA 4.6 wt% water). However, a relatively large share of CO_2 (0.7 wt%) seems unaccounted for in the PARC reaction product. For S-58 21d, 0.8 wt% water remains unallocated (calculated 2 wt%, vs. TGA 2.8 wt% water), although an overestimation was found in CO_2 (0.5 wt%). Table 11 presents the outcomes of the mass balance calculations for the hydration products = 100%.

The mass balance does not consider the volatiles because the SEM-EDX-based PARC data are inherently volatile-free. However, their values can be used to support the consistency of the calculated phase proportions in Table 11. The TGA-measured volatiles must reside in the PARC "Hydration product" or in the {Ca}-phase of PARC because all the starting material phases are volatile-free. Therefore, by knowing the

Table 10

Calculated phase composition of the PARC reaction product, by the mass balance (all Fe^{2+} was oxidized to Fe^{3+}) for sample S-16 21 d.

Phase	Reaction product	Hydrotalcite Pyroaurite $Mg_6Fe_2(CO_3)(OH)_{16} \cdot 4(H_2O)$		Hydrogarnet Fe-katoite $Ca_3(Al,Fe)_2(OH)_{12}$		Hibschite $Ca_3(Al,Fe)(SiO_4)_2(OH)_4$		C-S-H $Ca_{1.7}SiO_{3.7}\cdot 2\,H_2O$		Calc. total reaction product
Molar proportions (%)		8.3		19		22		51		*100*
Mass proportions (w.t %)		13.4		21.7		35.4		29.5		*100*
Measured	PARC	XRD		XRD				XRD		
Amount (wt%)	19.8	0.5		5.4				-		
LSQ (wt%)		2.7		4.3		7.1		5.9		*20*
Composition	Oxide (wt %)	Molar fractions	Oxide (wt%)	Molar fractions	Oxide (wt%)	Molar fractions	Oxide (wt%)	Molar fractions	Oxide (wt%)	
SiO_2 / Si^{4+}	17.11					1.64	22.1	0.82	31.1	
P_2O_5 / P^{5+}	1.9					0.16	2.5	0.08	3.5	
V_2O_5 / V^{5+}	1.3					0.08	1.6	0.04	2.3	
TiO_2 / Ti^{4+}	1.7					0.12	2.2	0.06	3.1	
$\Sigma M^{4+,5+}$						2		1		
Al_2O_3 / Al^{3+}	2.9	0.31	3.6	0.31	5.0	0.31	3.6			
Fe_2O_3 / Fe^{3+}	16.7	1.66	30	1.66	41.5	1.66	29.7			
Cr_2O_3 / Cr^{3+}	0.4	0.03	0.5	0.03	0.8	0.03	0.5			
ΣM^{3+}		2		2		2				
MgO / Mg^{2+}	5.4	4.39	40							
FeO / Fe^{2+}	6.3									
MnO / Mn^{2+}	3.5	1.61	25.9							
ΣM^{2+}		6								
CaO / Ca^{2+}	42.8			3.00	52.7	3.00	37.7	1.7	60	
Na_2O / Na^+	0.0									
K_2O / K^+	0.0									
$\Sigma M^{2+,1+}$				3		3		1.7		
Total (wt%)			100		100		100		100	
Total c.f.u. †		8		5		7		2.7		
H_2O allocated	23.3	12.0	48.9	6.0	33.9	2.0	8.1	2.0	22.7	4.68
CO_2 allocated	4.9	1.0	10	0.0	0.0	0.0	0.0	0.0	0.0	0.27
Molar mass volatile free (g/mol)		442		319		445		158		

† Cations per formula unit

Table 11

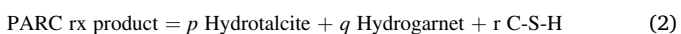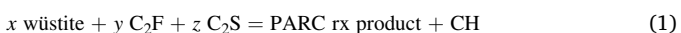The outcome of the mass balance calculations for the Hydration products = 100%.

Sample ID	Hydration product	=	Hydrotalcite Pyroaurite	+	Hydrogarnet Fe-katoite	Hibschite	+	C-S-H
S-16 21d	100%		13.40%		21.70%	35.40%		29.50%
S-58 21d	100%		9%		14.10%	24.40%		52%

volatile stoichiometric contents of the postulated hydration phases and using their calculated presence in the PARC reaction product, the volatile content of the PARC reaction product can be calculated.

Some unallocated water and CO_2 may have resided in the PARC {Ca}-phase. Considering uncertainties, such as 1) ongoing carbonation by ambient CO_2 of the hydrated slag powders, 2) the shown issue with representative area size and uncertainty in phase proportions in PARC, 3) the difficulty of quantitative Rietveld-XRD analysis of low amounts of poorly crystalline phases, and 4) the ambiguity of TGA interpretation, for example, which is the same range of the DTG peaks and which volatile/phase they correspond to, it is concluded that the volatiles are in reasonable agreement with the phase proportions from mass balance.

3.4.1. BOF slag hydration reaction equations

As shown in this work, the composition of the hydration reaction product of steel slag after 21 days of hydration is composed of contributions of the individual reactant phases, and it can be unraveled into its constituent product phases using mass balance calculations:

$$x \text{ wüstite} + y\,C_2F + z\,C_2S = \text{PARC rx product} + CH \quad (1)$$

$$\text{PARC rx product} = p \text{ Hydrotalcite} + q \text{ Hydrogarnet} + r \text{ C-S-H} \quad (2)$$

where x, y, z, p, q, and r are the unknown quantities of each phase.

Balance calculations of the equations were based on the mass contributions of phases not considering CO_2 and H_2O, given that the volatiles were not included in the SEM-EDX analysis. However, these mass balances are not the same as chemical reaction equations or reaction mechanisms, because there may be several reaction steps between the dissolution of the slag phases and the formation of the hydration products observed with SEM-EDX. Nevertheless, it is easier to understand the calculations if these mass proportions are translated from the mass balances into chemical reaction equations on a molar basis.

An equation with simplified phase notation formulas for each chemical reaction can be written scaled to one hydrogarnet and one hydrotalcite. In Eqs. (3), (4), (5), and (6), respectively, G, J, K, and N are the unknown reaction stoichiometry coefficients that express the relative proportion in which individual reactions contribute to the overall reaction.

Hydrogarnet formation:

$$G\,[C_2F + 2\,C_2S + H_{(9.6-2.3x)} = C_3FS_xH_{(3-x)2} + (1.7x\text{-}0.4)\,CH + (2\text{-}x)\,C_{1.7}SH_2] \quad (3)$$
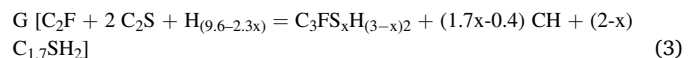
Hydrogarnet is expressed as $C_3FS_xH_{(3-x)2}$ representing the solid

solution between end-members C_3FH_6 and $C_3FS_2H_2$, where the amount of silica- incorporated into the hydrogarnet directly influences the amount of portlandite (CH) and C-S-H-gel formed. Fig. 8 demonstrates how the silica content "x" in the hydrogarnet formation is related to the amounts of C-S-H and portlandite formed. Per mol of hydrogarnet, with S_x given on the horizontal axis, the phase amounts formed of C-S-H and portlandite can be read on the vertical axis. The results for three different assumed C/S ratios (1.4, 1.7, and 2) in the C-S-H are presented. If x = 0, that is, a silica-free hydrogarnet (Fe-katoite, C_3FH_6) forms, and C/S= 2, then portlandite is consumed, which appears as a negative value in Fig. 8. If a value of C/S= 1.7 is assumed for the C-S-H phase, the value becomes less negative. For C/S= 1.4, portlandite forms in the reaction.

Hydrotalcite formation:

$$J\ [C_2F + 6\ M + 14\ H + c = M_6FcH_{12} + 2CH] \qquad (4)$$
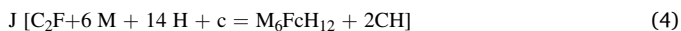
with c=CO_2.

Wüstite oxidation:

$$K\ [2\ f + 2CH = C_2F + 2\ H] \qquad (5)$$

with f=FeO.

It should be clear that oxidation is included as 2 f=F in the reaction. The wüstite oxidation reaction appears to have the effect of C_2F restoration. However, the reaction mechanism does not form C_2F during hydration. Preferably, the wüstite oxidation directly contributes to the hydrotalcite and hydrogarnet formation. In the overall set of reactions, it serves as a supplement to C_2F consumption.

C-S-H gel formation:

$$N\ [C_2S + 2.3\ H = C_{1.7}SH_2 + 0.3CH] \qquad (6)$$
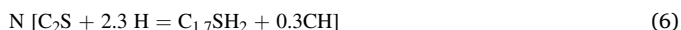
The overall reaction (as the sum of all the reactions above, assuming x = 1 and each reaction stoichiometry coefficient — G, J, K, and N — is set as 1) is read as:

$$C_2F + 3\ C_2S + 10Mf + 21.6\ H = C_3FSH_4 + M_6FcH_{12} + 1.6CH + 2\ C_{1.7}SH_2 \qquad (7)$$
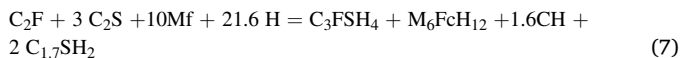
including the oxidation of 2 f=F.

The phase notation is simplified as in all reaction equations M is used for both MgO and MnO, S represents all cations interchangeable with Si^{4+} (P^{5+}, Ti^{4+}, and V^{4+} or V^{5+}), and F represents all trivalent cations (Al^{3+}, Fe^{3+}, Cr^{3+}). In addition to the product forming equations above, the oxidation of Fe^{2+}/FeO from the dissolving wüstite (Fe, Mg)O to Fe^{3+}/Fe_2O_3 during hydration is considered, whereby it is understood that the oxidation state of the MgO and MnO remains unaltered. When FeO oxidizes to Fe_2O_3, there is a mass gain of half an oxygen atom in the sample for each mole of FeO, which causes minor discrepancies between the mass and molar-based values. Furthermore, only the FeO component of the wüstite can oxidize, and Rietveld and PARC were used to determine the amount of Fe^{2+} (magnetite and wüstite amounts from QXRD, combined phase composition from PARC).

It should be clear that the mass balance-based equations (Eqs.1 and 2) cannot consider the oxidation state of iron because this value is unknown from the SEM-EDX analysis. As a first step, an approximation for the molar chemical reaction equation of the entire hydration process of BOF slag can be derived from the involved mass of phases, using their molar masses, as listed in Table 10. In a second step, the best-fit combination values of G, J, K, and N (Appendix B "Summary table rx") for this approximated molar chemical reaction can be calculated for each sample to derive stoichiometric values of reactants and hydration products in moles. Finally, the mass of reactants and products, as recalculated to moles (step 1), involved in the hydration reaction was compared to the stoichiometry of the reaction from the LSQ approximation (step 2) in Table 12. Note that values are derived for x ($0 \leq x \leq 2$), which is in the S_x of hydrogarnet ($C_3FS_xH_{(3-x)2}$), and all reaction contribution rates are scaled relative to 1 unit of C_2F.

The stoichiometry of the hydrogarnet demonstrates reasonable agreement between mass-based and balanced molar-based reactions.

Table 13 also shows that a significant amount of C_2S was involved in the mass balance of the coarse slag. Consequently, C_2S became dominant in the chemical reaction equation because relatively minor amounts of C_2F were involved, and the reaction was scaled to $C_2F = 1$, increasing the other phases.

The chemical reaction equations indicate a trade-off between C_2S contributing to increasing the silica content in the hydrogarnet and increasing the amount of C-S-H gel in the reaction product, influenced by the amount of iron oxidation. For S-58, the amount of hydrotalcite (pyroaurite) appears higher in the stoichiometric reaction equation compared to the mass-based calculation.

For ease of comparison to the extent of hydration reaction in the two 21-day samples and coming full circle round, the calculated phase amounts (mass) from the balanced stoichiometric reaction equations (Table 12 row B) are compared to the derived values from PARC in Table 13. The details of the calculations can be found in Appendix B ("S58 overall rx" and "S16 overall rx").

The discrepancy between the observed portlandite (PARC) and the amount involved in the balanced reaction equation is most noticeable in Table 13. The following explanations come to mind for the deviation between reaction stoichiometry and observed for portlandite phase amounts: (1) the invoked wüstite oxidation reaction with consumption of CH leading to hydrogarnet formation acts to a lesser extent than the LSQ optimized reaction balance calculation. For example, small amounts of amorphous goethite may have been formed [76]. (2) The hydrogarnet contains more silica than that calculated with the LSQ-optimized reaction balance, meaning there should be less C-S-H formation and more CH (Fig. 8). (3) The C-S-H has a lower C/S ratio. In the calculations, C/S = 1.7 was imposed [78], but it could be lower, for example, C/S= 1.4, yielding more portlandite (Fig. 8). However, the low C/S values were incompatible with the observed portlandite phase presence. (4) There is additional C_2S hydration, locally around the C_2S crystals, for which the products were not incorporated into the newly formed hydration reaction products. (5) Some of the PARC {Ca} phase is calcite rather than portlandite.

The first four explanations would raise the portlandite content of the samples, and the last one would explain the additional CO_2 (from TGA) and act to decrease the discrepancy.

3.5. Potential immobilization of heavy metals

The BOF slag used in this study contains chromium and vanadium (see Table 1), implying a potential risk of leaching when applying the material. Cr is mostly incorporated in the wüstite and brownmillerite phases, while V is incorporated into brownmillerite and C_2S [22,26], as shown in Table 3. The one-batch leaching test was performed to evaluate the environmental impact and capacity of the hydration products to immobilize the heavy metals. The results are presented in Table 14. For the non-hydrated BOF slag, V and Cr, leaching was well within legal limits, with S-16 leaching slightly less than S-58, which was unexpected considering its higher surface area.

After hydrating S-16 and S-58 for 21 days, the leaching of Cr was reduced in both samples, while V leaching slightly increased in S-58, although it was below the detection limit in S-16. The limited leaching, together with the high content of V in the hydration products (Table 6) in the dominant subregion, clearly shows that Cr and V are well immobilized not only in the hydrogarnet [79], as observed previously, but also in the C-S-H phase structure, which explains the differences in V leaching. S-16 had a higher reaction degree after 21d and, therefore, could immobilize more V while simultaneously increasing the leachate pH to 12.6 as an effect of its portlandite. S-58, on the contrary, has formed insufficient portlandite during the 21d hydration to maintain a high pH in the leachate. Therefore, the pH decreased, and V-leaching slightly increased. The effect of pH on V-leaching from BOF-slag has

Table 12
Calculated mass balance-based molar reaction stoichiometry and best fit to the 4 reaction equations for the hydrated samples S-16 21d and S-58 21d. A= Mass balance-based molar reaction, and B = Best fit molar reaction stoichiometry.

Sample/ Mineral phases		Stoichiometry coefficient				Reactant					Product					
		G	J	K	N	C_2F	C_2S	M+f	f	H	$C_3FS_0H_6$	$C_3FS_2H_2$	x value	M_6FcH_{12}	$C_{1.7}SH_2$	CH
A	S-16	-	-	-	-	1	3.42	4.38		14.4	0.77	0.9	1.08	0.34	2.11	
	S-58	-	-	-	-	1	15.48	11.11		48.06	1.68	2.07	1.11	0.75	12.44	
B	S-16	1.46	0.25	0.71	0.57	1	3.49	4.38	1.43	14.12	0.73	0.72	0.99	0.25	2.04	1.13
	S-58	3.12	0.27	2.39	9.35	1	15.6	11.16	4.78	42.91	1.48	1.64	1.05	0.27	12.32	2.89

Table 13
Product phase based on stoichiometric reaction equations (Reaction), compared to PARC reaction mass balance based (PARC) in wt%.

Sample/Mineral phase		Hydrogarnet	Hydrotalcite	Portlandite	C-S-H	Total Product
S-16 21d	Reaction	11.2	2.3	1.3	6.5	21.3
	PARC	11.4	2.7	5.4	5.9	25.4
S-58 21d	Reaction	3.2	0.3	0.4	5.2	9.2
	PARC	3.4	0.8	3.3	4.6	12.1

Note: Mass scaled to wt% PARC. The reaction product excludes portlandite.

Table 14
Leaching of contaminants measured by one-stage batch leaching test and the SQD limit values (mg/kg).

Sample	pH	Chromium (Cr)	Vanadium (V)
S-58	11.56	0.042	0.678
S-16	11.58	0.034	0.190
S-58 21d	11.48	0.037	0.829
S-16 21d	12.62	0.025	< 0005
SQD legislation limits		0.630	1.800

been well documented [80].

The BOF slag has low reactivity and will require intense milling, expectedly to particle sizes below 15 μm, or (SSA> 1.5 m²/g), to achieve practical degrees of hydration. A low water demand should be considered if it is used as a binder. When more water is used than is chemically necessary to hydrate the BOF slag, the remaining free water will introduce porosity to the sample, potentially lowering the strength and causing drying shrinkage and cracking [81].

Based on the above experimental findings, it is reasonable to believe that the new hydration products can reduce the leaching of chromate and vanadate by immobilizing them in hydration products that are stable at low temperatures. The immobilization effects of Cr and V in BOF slag will continue to be explored in the near future.

4. Conclusions

For two BOF slag samples with different particle sizes — D(50) of 16 μm (S-16) and 58 μm (S-58) — a link was established between mineralogy, particle size, the extent of hydration, and the immobilization of heavy metals using in-depth characterization:

Both samples contained amorphous matter before hydration, which compositionally corresponded largely to C_2S and was increased in relative amount by milling. Hydrating the two BOF slag samples in water initially led to the formation of crystalline hydration products hydrogarnet, hydrotalcite, and portlandite at the expense of amorphous matter. All major slag phases, including wüstite, participated in the reaction. After 14 days, the amorphous content continuously increased up to 90 days. The total bound water after 21d of hydration was 4.05% and 6.28% in the samples S-58 and S-16, reaching degrees of hydration of 15% and 29%, respectively, showing that the hydraulic properties were significantly improved by milling.

Combining PARC with QXRD, it was found that less than one-third of the hydration product was detected as crystalline, whereas the rest was amorphous. Based on our observations, it is postulated that the

hydration product consists of three distinct phases that are poorly crystalline to X-ray amorphous and inter-grown on a submicron scale, which cannot be resolved with SEM-EDX Spectral Imaging. These phases are a ferric-hydrogarnet, a ferric-hydrotalcite, and a C-S-H gel phase with assumed $C_{1.7}SH_2$ stoichiometry. In terms of these three phases, the make-up of the hydration products was determined using mass balance calculations. In addition, the silica content in the hydrogarnet $C_3(AF)$ $S_xH_{(3-x)*2}$ solid solution and the contribution of the original slag phases to the formation of the hydration product were calculated for each sample.

A reaction equation is proposed showing that hydrogarnet forms from C_2F and C_2S during the first 7 days of hydration and that there is a trade-off between the silica content of the hydrogarnet and the amount of C-S-H formed. Divalent Mg, Mn, and Fe from wüstite control the hydrotalcite formation. However, interestingly, the oxidation of Fe^{2+} from wüstite to Fe^{3+}, in a reaction consuming portlandite, also contributes to hydrogarnet formation. For S-58, the best set of balanced reaction equations demonstrated a much higher consumption of C_2S and more C-S-H phase formation.

The limited leaching of heavy metals from the hydrated sample S-16 21d and the high content of vanadium in the hydration product evinces that the heavy metals Cr and V are well retained by the hydration products. In addition, the smaller particle size of S-16 and its higher reactivity played an important role in the immobilization capacity.

Environmental implication

Chromium (Cr) and vanadium (V) are present in BOF slag. The potential leaching of Cr and V out to the environment being extremely toxic to animals and humans, causing cancer, skin and breathing problems. The C_2S phase in the BOF slag can incorporate V ions, while the phases wüstite and brownmillerite can incorporate Cr. The C_2S and the other major phases in BOF slag will react forming hydration products like C-S-H gel, portlandite and hydrogarnets. The solubility, and reactivity capacity of the initial phases and the percentage of hydration products formed, as well as their composition will contribute to the potential immobilization of the heavy metals.

CRediT authorship contribution statement

W. F. Santos: Conceptualization, Methodology, Validation, Investigation, Writing – original draft, Visualization. **K. Schollbach:** Methodology, Investigation, Writing – review & editing, Visualization, Supervision. **S. Melzer:** Methodology, Writing – review & editing. **S. van der Laan:** Conceptualization, Methodology, Validation,

Investigation, Resources, Writing – review & editing, Project administration. **H.J.H. Brouwers:** Conceptualization, Resources, Writing – review & editing, Project administration.

Declaration of Competing Interest

The authors declare that they have no known competing financial interests or personal relationships that could have appeared to influence the work reported in this paper.

Data Availability

Data will be made available on request.

Acknowledgement

Appendix A. Supporting information

Supplementary data associated with this article can be found in the online version at doi:10.1016/j.jhazmat.2023.131029.

References

[1] Zhao, J., Yan, P., Wang, D., 2017. Research on mineral characteristics of converter steel slag and its comprehensive utilization of internal and external recycle. J Clean Prod 156, 50–61. https://doi.org/10.1016/j.jclepro.2017.04.029.

[2] Małolepszy, J., Deja, J., Brylicki, W., 1997. Durability of mortars and concrete containing ground converted slag. IV CANMET/Acids Int Conf Durab Concr C 189–206.

[3] C. Shi, Steel Slag — Its Production, Processing, Characteristics, and Cementitious Properties, (2004) 230–236.

[4] Yildirim, I.Z., Prezzi, M., 2015. Steel slag: Chemistry, mineralogy, and morphology. Geotech Spec Publ GSP 256, 2816–2825. https://doi.org/10.1061/9780784479087.263.

[5] The European Slag Association, Position paper on the Status of Ferrous Slag complying with the Waste Framework Directive and the REACH Regulation, 2012.

[6] Global Slag, 2021. 2020 steel production falls by 1% globally. Glob Slag N. ⟨https://www.globalslag.com/news/item/257-2020-steel-production-falls-by-1-globally⟩.

[7] Reddy, A.S., Pradhan, R.K., Chandra, S., 2006. Utilization of basic oxygen furnace (BOF) slag in the production of a hydraulic cement binder. Int J Miner Process 79, 98–105. https://doi.org/10.1016/j.minpro.2006.01.001.

[8] Wang, Q., Yan, P., 2010. Hydration properties of basic oxygen furnace steel slag. Constr Build Mater 24, 1134–1140. https://doi.org/10.1016/j.conbuildmat.2009.12.028.

[9] Lee, H.S., Lim, H.S., Ismail, M.A., 2017. Quantitative evaluation of free CaO in electric furnace slag using the ethylene glycol method. Constr Build Mater 131, 676–681. https://doi.org/10.1016/j.conbuildmat.2016.11.047.

[10] Wang, Q., Wang, D., Zhuang, S., 2017. The soundness of steel slag with different free CaO and MgO contents. Constr Build Mater 151, 138–146. https://doi.org/10.1016/j.conbuildmat.2017.06.077.

[11] Cheng, H., Yi, H., Wang, J., Wan, Y., Xu, G., Chen, H., 2012. An Overview of Utilization of Steel Slag. Procedia Environ Sci 16, 791–801. https://doi.org/10.1016/j.proenv.2012.10.108.

[12] Slag recycling: valuable by- products, Recover. -Recycling Technol. World Wild. (2020). ⟨https://www.recovery-worldwide.com/en/artikel/slag-recycling_3528047.html⟩.

[13] Scrivener, K.L., John, V.M., Gartner, E.M., 2018. Eco-efficient cements: potential economically viable solutions for a low-CO₂ cement-based materials industry. Cem Concr Res 114, 2–26. https://doi.org/10.1016/J.CEMCONRES.2018.03.015.

[14] Guo, J., Bao, Y., Wang, M., 2018. Steel slag in China: treatment, recycling, and management. Waste Manag 78, 318–330. https://doi.org/10.1016/J.WASMAN.2018.04.045.

[15] Jiang, Y., Ling, T.C., Shi, C., Pan, S.Y., 2018. Characteristics of steel slags and their use in cement and concrete—a review. Resour Conserv Recycl 136, 187–197. https://doi.org/10.1016/j.resconrec.2018.04.023.

[16] Martins, A.C.P., Franco de Carvalho, J.M., Costa, L.C.B., Andrade, H.D., de Melo, T. V., Ribeiro, J.C.L., et al., 2021. Steel slags in cement-based composites: an ultimate review on characterization, applications and performance. Constr Build Mater 291. https://doi.org/10.1016/j.conbuildmat.2021.123265.

[17] Ahmed, M.J., Santos, W.F., Brouwers, H.J.H., 2023. Air granulated basic Oxygen furnace (BOF) slag application as a binder: effect on strength, volumetric stability, hydration study, and environmental risk. Constr Build Mater 367, 130342. https://doi.org/10.1016/j.conbuildmat.2023.130342.

[18] Jiang, Y., Ling, T.C., Shi, C., Pan, S.Y., 2018. Characteristics of steel slags and their use in cement and concrete—a review. Resour Conserv Recycl 136, 187–197. https://doi.org/10.1016/j.resconrec.2018.04.023.

[19] Chaurand, P., Rose, J., Domas, J., Bottero, J.Y., 2006. Speciation of Cr and V within BOF steel slag reused in road constructions. J Geochem Explor. https://doi.org/10.1016/j.gexplo.2005.08.006.

[20] Pan, S.Y., Chung, T.C., Ho, C.C., Hou, C.J., Chen, Y.H., Chiang, P.C., 2017. CO₂ mineralization and utilization using steel slag for establishing a waste-to-resource supply chain. Sci Rep 7, 1–11. https://doi.org/10.1038/s41598-017-17648-9.

[21] Jiang, Y., Ling, T., Shi, C., Pan, S., 2018. Resources, Conservation & Recycling Characteristics of steel slags and their use in cement and concrete — a review. Resour Conserv Recycl 136, 187–197. https://doi.org/10.1016/j.resconrec.2018.04.023.

[22] Kaja, A.M., Schollbach, K., Melzer, S., van der Laan, S.R., Brouwers, H.J.H., Yu, Q., 2021. Hydration of potassium citrate-activated BOF slag. Cem Concr Res 140, 106291. https://doi.org/10.1016/j.cemconres.2020.106291.

[23] van Zomeren, A., van der Laan, S.R., Kobesen, H.B.A., Huijgen, W.J.J., Comans, R. N.J., 2011. Changes in mineralogical and leaching properties of converter steel slag resulting from accelerated carbonation at low CO₂ pressure. Waste Manag 31, 2236–2244. https://doi.org/10.1016/j.wasman.2011.05.022.

[24] van Hoek, C., Small, J., van der Laan, S., 2016. Large-area phase mapping using phase recognition and characterization (PARC) software. Micros Today 24, 12–21. https://doi.org/10.1017/S1551929516000572.

[25] Belhadj, E., Diliberto, C., Lecomte, A., 2012. Characterization and activation of basic oxygen furnace slag. Cem Concr Compos 34, 34–40. https://doi.org/10.1016/j.cemconcomp.2011.08.012.

[26] Ahmed, M.J., Cuijpers, R., Schollbach, K., v.d. Laan, S., Brouwers, H.J.H., 2022. V and Cr substitution in dicalcium silicate (C2S) under oxidizing and reducing conditions- Synthesis, reactivity, and leaching behaviour studies. J Hazard Mater. https://doi.org/10.1016/j.jhazmat.2022.130032.

[27] K. Scrivener, R. Snellings, B. Lothenbach, F. Group, A Practical Guide to Microstructural Analysis of Cementitious Materials Edited by, n.d.

[28] Scrivener, K.L., Fu, T., Gallucci, E., Walenta, G., Bermejo, E., 2004. Quantitative study of Portland cement hydration by X-ray diffraction. Rietveld Anal Indep Methods 34, 1541–1547. https://doi.org/10.1016/j.cemconres.2004.04.014.

[29] C. Yang, S. Wu, J. Xie, S. Amirkhanian, Q. Liu, J. Zhang, Y. Xiao, Z. Zhao, H. Xu, N. Li, F. Wang, L. Zhang, Enhanced induction heating and self-healing performance of recycled asphalt mixtures by incorporating steel slag, 366 (2022). doi:10.1016/j.jclepro.2022.132999.

[30] Cui, Y., Wu, S., Xiao, Y., Hu, R., Yang, T., 2021. Environmental performance and functional analysis of chip seals with recycled basic oxygen furnace slag as aggregate. J Hazard Mater 405, 124441. https://doi.org/10.1016/j.jhazmat.2020.124441.

[31] Kriskova, L., Pontikes, Y., Cizer, Ö., Mertens, G., Veulemans, W., Geysen, D., et al., 2012. Effect of mechanical activation on the hydraulic properties of stainless steel slags. Cem Concr Res 42, 778–788. https://doi.org/10.1016/j.cemconres.2012.02.016.

[32] Yashima, S., Kanda, Y., Sano, S., 1987. Relationships between particle size and fracture energy or impact velocity required to fracture as estimated from single particle crushing. Powder Technol 51, 277–282. https://doi.org/10.1016/0032-5910(87)80030-X.

[33] Zhu, X., Hou, H., Huang, X., Zhou, M., Wang, W., 2012. Enhance hydration properties of steel slag using grinding aids by mechanochemical effect. Constr Build Mater 29, 476–481. https://doi.org/10.1016/j.conbuildmat.2011.10.064.

[34] J. Hou, J. Liu, Hydration activity and mechanical properties of steel slag used as cementitious materials, (2022). doi:10.1002/ep.13756.

[35] Alam, Q., Schollbach, K., van Hoek, C., van der Laan, S., de Wolf, T., Brouwers, H.J. H., 2019. In-depth mineralogical quantification of MSWI bottom ash phases and their association with potentially toxic elements. Waste Manag 87, 1–12. https://doi.org/10.1016/j.wasman.2019.01.031.

[36] van Hoek, C., Small, J., van der Laan, S., 2016. Large-Area Phase Mapping Using P h A se R ecognition and C haracterization (PARC) Software. Micros Today 24, 12–21. https://doi.org/10.1017/s1551929516000572.

[37] Brunauer, S., Emmett, P.H., 1937. The use of low temperature van der waals adsorption isotherms in determining the surface areas of various adsorbents. J Am Chem Soc 59, 2682–2689. https://doi.org/10.1021/ja01291a060.

[38] B. Lothenbach, K. Scrivener, R. Snellings, A practical guide to microstructural analysis of cementitious materials, 2016.

[39] Coelho, A.A., 2018. TOPAS and TOPAS-Academic: an optimization program integrating computer algebra and crystallographic objects written in C++: An. J Appl Crystallogr 51, 210–218. https://doi.org/10.1107/S1600576718000183.

[40] Gualtieri, A.F., 2000. Accuracy of XRPD QPA using the combined Rietveld ± RIR method research papers. J Appl Crystallogr 33, 267–278. https://doi.org/10.1107/S002188989901643X.

[41] Schollbach, K., v.d. Laan, S., 2021. Microstructure analysis with quantitative phase mapping using SEM-EDSand Phase Recognition and Characterization (PARC) Software: appliedto steelmaking slag. In: Pollmann, H (Ed.), Ind. Waste. DE GRUYTER, Halle, pp. 57–96. https://doi.org/10.1515/9783110674941-203.

[42] Kocaba, V., Gallucci, E., Scrivener, K.L., 2012. Methods for determination of degree of reaction of slag in blended cement pastes. Cem Concr Res 42, 511–525. https://doi.org/10.1016/j.cemconres.2011.11.010.

[43] EN, EN 12457–2:2002 - Characterization of waste - Leaching - Compliance test for leaching of granular, (2002).

[44] Dutch Government, Regeling bodemkwaliteit - Dutch Soil Decree - Appendix A, (2007).

[45] B.H. Toby, R factors in Rietveld analysis: How good is good enough ?, (2006) 67–70. doi:10.1154/1.2179804.

[46] Post, J., Bish, D., 1989. Rietveld refinement of crystal structures using powder X-ray diffraction data. Mineral Soc Am 20, 277–308.

[47] Thomas, C., Rosales, J., Polanco, J.A., Agrela, F., 2019. 7. Steel slags. Elsevier Ltd. https://doi.org/10.1016/B978-0-08-102480-5.00007-5.

[48] Weeber, A.W., Bakker, H., 1988. Amorphization by ball milling. A review. Phys B Phys Condens Matter 153, 93–135. https://doi.org/10.1016/0921-4526(88)90038-5.

[49] Scarlett, N.V.Y., Madsen, I.C., 2018. Effect of microabsorption on the determination of amorphous content via powder X-ray diffraction. Powder Diffr 33, 26–37. https://doi.org/10.1017/S0885715618000052.

[50] Pietsch, Wolfgang B., 2008. Undesired and Desired Agglomeration. In: Agglom. Process. Phenomena, Technol. Equip. Wiley-VCH, Naples, FL, p. 622.

[51] Kim, Y.M., Hong, S.H., 2004. Influence of minor ions on the stability and hydration rates of β-dicalcium silicate. J Am Ceram Soc 87, 900–905. https://doi.org/10.1111/j.1551-2916.2004.00900.x.

[52] Gineys, N., Aouad, G., Sorrentino, F., Damidot, D., 2011. Incorporation of trace elements in Portland cement clinker: Thresholds limits for Cu, Ni, Sn or Zn. Cem Concr Res 41, 1177–1184. https://doi.org/10.1016/J.CEMCONRES.2011.07.006.

[53] Tromans, D., Meech, J.A., 2001. Enhanced dissolution of minerals: stored energy, amorphism and mechanical activation. Miner Eng 14, 1359–1377. https://doi.org/10.1016/S0892-6875(01)00151-0.

[54] Rozov, K., Berner, U., Taviot-gueho, C., Leroux, F., Renaudin, G., Kulik, D., et al., 2010. Cement and concrete research synthesis and characterization of the LDH hydrotalcite – pyroaurite solid-solution series. Cem Concr Res 40, 1248–1254. https://doi.org/10.1016/j.cemconres.2009.08.031.

[55] Dilnesa, B.Z., Wieland, E., Lothenbach, B., Dähn, R., Scrivener, K.L., 2014. Cement and Concrete Research Fe-containing phases in hydrated cements. Cem Concr Res 58, 45–55. https://doi.org/10.1016/j.cemconres.2013.12.012.

[56] Dilnesa, B.Z., Lothenbach, B., Renaudin, G., Wichsher, A., Kulik, D., 2013. Synthesis and characterization of hydrogarnet Ca3(AlxFe1-x)2(SiO4)y(OH)4(3-y). Cem Concr Res 96–111. https://doi.org/10.1016/j.cemconres.2014.02.001.

[57] Taylor, H.F.W., 1998. Hydration of Portland cement. In: Telford (Ed.), Cem. Chem., Thomas Tel. Academic press, London, pp. 187–225.

[58] Li, J., Yu, Q., Wei, J., Zhang, T., 2011. Structural characteristics and hydration kinetics of modified steel slag. Cem Concr Res 41, 324–329. https://doi.org/10.1016/j.cemconres.2010.11.018.

[59] Wang, Q., Yan, P., 2010. Hydration properties of basic oxygen furnace steel slag. Constr Build Mater 24, 1134–1140. https://doi.org/10.1016/j.conbuildmat.2009.12.028.

[60] E. Belhadj, C. Diliberto, A. Lecomte, Cement & Concrete Composites Characterization and activation of Basic Oxygen Furnace slag, 34 (2012) 34–40. doi:10.1016/j.cemconcomp.2011.08.012.

[61] Wang, S., Wang, C., Wang, Q., Liu, Z., Qian, W., Jin, C., et al., 2018. Study on cementitious properties and hydration characteristics of steel slag, 27, 357–364. https://doi.org/10.15244/pjoes/74133.

[62] Qian, G.R., Sun, D.D., Tay, J.H., Lai, Z.Y., 2002. Hydrothermal reaction and autoclave stability of Mg bearing RO phase in steel slag. Br Ceram Trans 101, 159–164. https://doi.org/10.1179/096797802225003415.

[63] Cuberos, A.J.M., De la Torre, Á.G., Martín-Sedeño, M.C., Moreno-Real, L., Merlini, M., Ordónez, L.M., et al., 2009. Phase development in conventional and active belite cement pastes by Rietveld analysis and chemical constraints. Cem Concr Res 39, 833–842. https://doi.org/10.1016/j.cemconres.2009.06.017.

[64] Palmer, S.J., Spratt, H.J., Frost, R.L., 2009. Thermal decomposition of hydrotalcites with variable cationic ratios. J Therm Anal Calor 95, 123–129. https://doi.org/10.1007/s10973-008-8992-4.

[65] Lothenbach, B., Durdzi, P., 2016. Thermogravimetric analysis. In: A Pract. Guid. to Microstruct. Anal. Cem. Mater, pp. 177–208.

[66] Stepkowska, E.T., 2005. Hypothetical transformation of Ca(OH)2 into CaCO3 in solid-state reactions of portland cement. In: J. Therm. Anal. Calorim, 80, pp. 727–733. https://doi.org/10.1007/s10973-005-0721-7.

[67] Ruiz-Agudo, E., Kudłacz, K., Putnis, C.V., Putnis, A., Rodriguez-Navarro, C., 2013. Dissolution and carbonation of portlandite [Ca(OH)2] single crystals. Environ Sci Technol 47, 11342–11349. https://doi.org/10.1021/es402061c.

[68] Galan, I., Glasser, F.P., Baza, D., Andrade, C., 2015. Assessment of the protective effect of carbonation on portlandite crystals. Cem Concr Res 74, 68–77. https://doi.org/10.1016/j.cemconres.2015.04.001.

[69] Nedeljković, M., Ghiassi, B., Melzer, S., Kooij, C., van der Laan, S., Ye, G., 2018. CO2 binding capacity of alkali-activated fly ash and slag pastes. Ceram Int 44, 19646–19660. https://doi.org/10.1016/j.ceramint.2018.07.216.

[70] Chen, W., 2007. Hydration of slag cement. Theory, Model Appl 1–241.

[71] Rozov, K., Berner, U., Taviot-Gueho, C., Leroux, F., Renaudin, G., Kulik, D., et al., 2010. Synthesis and characterization of the LDH hydrotalcite–pyroaurite solid-solution series. Cem Concr Res 40, 1248–1254. https://doi.org/10.1016/J.CEMCONRES.2009.08.031.

[72] Taylor, H.F.W., 1997. Cement chemistry. Cem Chem. https://doi.org/10.1680/cc.25929.

[73] Vespa, M., Wieland, E., Dähn, R., Lothenbach, B., 2015. Identification of the thermodynamically stable Fe-containing phase in aged cement pastes. J Am Ceram Soc 98, 2286–2294. https://doi.org/10.1111/jace.13542.

[74] Hong, S.Y., Glasser, F.P., 2004. Phase relations in the CaO-SiO2-H2O system to 200 °C at saturated steam pressure. Cem Concr Res 34, 1529–1534. https://doi.org/10.1016/j.cemconres.2003.08.009.

[75] Cuesta, A., De la Torre, Á.G., Santacruz, I., Diaz, A., Trtik, P., Holler, M., et al., 2019. Quantitative disentanglement of nanocrystalline phases in cement pastes by synchrotron ptychographic X-ray tomography. IUCrJ 6, 473–491. https://doi.org/10.1107/s2052252519003774.

[76] Mancini, A., Wieland, E., Geng, G., Dähn, R., Skibsted, J., Wehrli, B., et al., 2019. Fe(III) uptake by calcium silicate hydrates. Appl Geochem, 104460. https://doi.org/10.1016/j.apgeochem.2019.104460.

[77] Goldschmidt, V., 1937. The principles of distribution of chemical elements. J Chem Soc 655–673.

[78] H.J.H. Brouwers, A Hydration Model of Portland Cement using the work of Powers and Brownyard., Portland C, Eindhoven University of Technology, 2011. http://www.cement.org.

[79] R. Brydson, E. Paterson, Hydrogarnet: A Host Phase for Cr (VI) in Chromite Ore Processing Residue (COPR) and Other High pH Wastes, 41 (2007) 1921–1927.

[80] Hobson, A.J., Stewart, D.I., Bray, A.W., Mortimer, R.J.G., Mayes, W.M., Rogerson, M., et al., 2017. Mechanism of vanadium leaching during surface weathering of basic oxygen furnace steel slag blocks: a microfocus X-ray absorption spectroscopy and electron microscopy study. Environ Sci Technol 51, 7823–7830. https://doi.org/10.1021/ACS.EST.7B00874/SUPPL_FILE/ES7B00874_SI_001.PDF.

[81] K. Mehta, P.J.M. Monteiro, Concrete: Microstructure, Properties, and Materials, 4th ed., McGraw Hill, 2013.